Title

Numerical experiments on the convergence properties of state-based peridynamic laws and influence functions in two-dimensional problems

Authors

Queiruga, Alejandro F
Moridis, George

Publication Date

2017-08-01

DOI

10.1016/j.cma.2017.04.016

Peer reviewed

Numerical experiments on the convergence properties of state-based peridynamic laws and influence functions in two-dimensional problems

Author links open overlay panelAlejandro F.QueirugaGeorgeMoridis
Show more

https://doi.org/10.1016/j.cma.2017.04.016Get rights and content

Highlights

- Three state-based peridynamic laws and multiple influence functions are tested on static problems.
- The dilation state based models do not converge for every constant-strain problem.
- The deformation gradient model converges linearly but is unstable.
- A cubic influence function provides convergence for the most cases.
- All three models can achieve within 5% accuracy to the thin crack problem analytical solution.

Abstract

Peridynamics is widely used as the theoretical basis for numerical studies of fracture evolution, propagation, and behavior. While the theory has been shown to converge to continuum mechanics in the theoretical limit, its behavior as a discrete numerical approximation with respect to classic problems has not been shown. In this study, we use standard analytical solutions to thoroughly test the numerical accuracy and rate of convergence of the spatial discretization obtained by peridynamics. We analyze the accuracy and rate of convergence of three different peridynamic constitutive responses: of these, two involve a state-based dilation, and the third is based on the estimation of the deformation gradient. Additionally, we study the choice of the peridynamic influence

function in each of the constitutive responses. The peridynamic materials are solved in the linear elastic regime by solving a linear system of equations obtained by symbolically differentiating the force states. We test the methods against standard constant-strain solutions for uniaxial compression, isotropic compression, and simple shear. We also apply the methods to a finite material with a pressurized thin crack, using the Westergaard's solution method to obtain an analytical displacement field for comparison. The two dilation-based peridynamic constitutive responses are found to only converge to one of the constant strain solutions, while the deformation gradient-based law converges in all cases with an appropriate choice of the influence functions. We show that a cubic influence function is the best choice of those considered in all methods. Only the deformation gradient-based model converges for all three linear deformation problems, but is less accurate than the dilation-based models for the thin crack problem because of instabilities. We demonstrate an ad hoc smoothing technique based on the influence function that is able to alleviate these instabilities and improve the accuracy of the deformation gradient-based model.

Keywords

Peridynamics
Linear fracture mechanics
Convergence

1. Introduction

Peridynamics is an alternative formulation of mechanics based upon satisfying an integro-differential equation so as to avoid taking spatial derivatives [1]. Numerical models based on peridynamics are thus well-suited to problems involving discontinuities, such as plasticity, fracture propagation, and high-speed impacts. The criteria governing fracture growth in peridynamics are usually based upon the displacement field solution in the form of the bond stretches [2], [3]. This work closely examines the accuracy of the displacements obtained by three forms for the peridynamics force–density response in static linear elastic problems with known analytical solutions. We combine the three responses with different selections of the peridynamic influence function and determine the order of convergence of the models when independently refining the grid point discretization and the relative size of the peridynamic horizon.

1.1. Background

In the theoretical framework of peridynamics, each point in the material has a response based on the integral of force densities from neighboring material points, without taking any derivatives of the mechanical fields [1]. In practical implementation, the material is discretized as a finite set of points (or particles), and the summation of force density laws from in-range material points is used to solve the equations of motion of the particle. As illustrated in Fig. 1, the material points are connected to a finite number of other particles using an influence function wr with a compact support of radius δ which covers the region known as the peridynamic horizon, Hx. Discontinuities are naturally incorporated by assigning a damage field to the bonds between the finite material points that weights the interaction force densities.

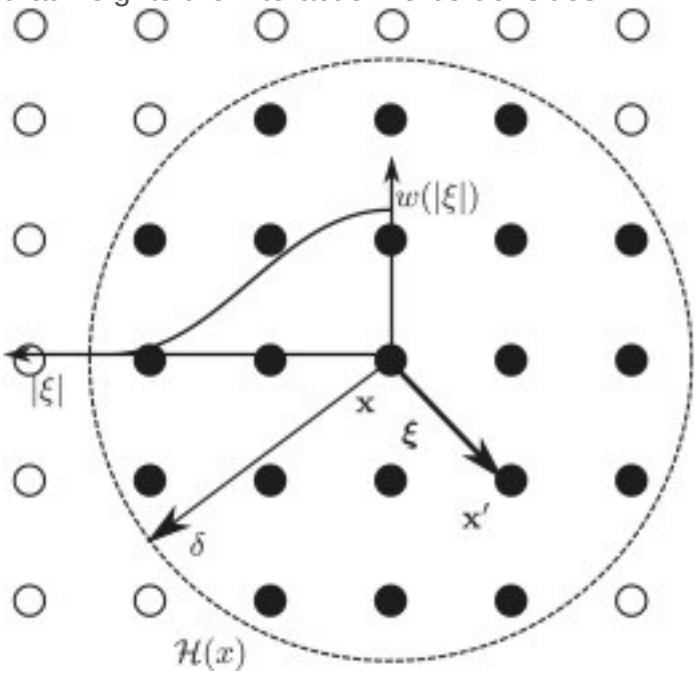

1. Download high-res image (145KB)
2. Download full-size image

Fig. 1. The horizon H(x) at a particle x and the peridynamic influence function w(r) as a function of the magnitude of the distance vector ξ between particles x and x′. A cubic-spline influence function centered on the particle x is illustrated. Shaded particles are inside of the horizon.

Unlike traditional methods, such as the finite element method, this underlying theoretical framework is different from continuum mechanics. This difference requires further investigation to assert that the numerical models developed with peridynamics are consistent with traditional results in mechanics. The peridynamic balance of linear momentum has been shown to converge to the continuum mechanic partial differential equation as the horizon size collapses to a point [4], [5]. On the other end, peridynamics

has been interpreted as a coarsening of molecular dynamics to be applied to those smaller length scales [6]. While the nonlocal nature of peridynamics may be useful in capturing microscale behavior, we are interested in the applicability of computationally practical discretizations and horizon sizes to macroscopic problems.

1.2. Literature review

Peridynamics has been used extensively to simulate problems focusing fracture mechanics. A common test problem for peridynamic models is a projectile impacting and shattering a brittle disk [7], [8], [9]. Lai, 2014 used a peridynamic model based on a traditional continuum mechanics constitutive law to simulate the fracturing of geomaterials under high-speed impact loads [10]. The original formulation modeled a brittle linear elastic solid [1], but the theory has been extended to more complex materials. Peridynamic responses have been developed to predict failure in materials with complex microstructures, such as anisotropic materials [11] and laminates [12], [13]. Viscoplastic constitutive responses were incorporated into the peridynamic framework in Foster, 2010 to model the plastic deformation of a metal cylinder under impact [14]. Turner, 2012 developed a peridynamic constitutive response for porous materials that are be applied to geotechnical subsidence problems [15]. Peridynamics theory has also been applied to physics beyond mechanics. Thermal diffusion has been cast into the nonlocal interaction framework of peridynamics to solve coupled thermo-mechanical problems [2], [16]. Katiyar, 2013 developed a peridynamic model for porous flow that corresponds to the continuum Darcian flow partial differential equation in the peridynamic vanishing horizon limit [17]. The hydraulic fracture process has been simulated in an entirely peridynamics framework with fully coupled flow and mechanics in Ouchi, 2015 [18].

1.3. Approach in this study

The core of the theoretical model is the force density constitutive response that governs the interaction between material points. The original bond-based peridynamic model uses a force density expression that only depends on two points, and consequently suffered from the restriction of a fixed Poisson ratio [19]. A number of schemes to remove this restriction have been proposed. Liu, 2012 included a lateral force to bonds on boundary particles to represent the Poisson effect [20]. Gerstle, 2007 added a rotational degree of freedom to the bond-based force densities, resulting in a truss-like formulation [21]. Further work has involved extending peridynamic force density calculations to depend on the deformation of the entire horizon, enabling an even

greater range of constitutive behavior to be captured [19]. This yields state-based peridynamic models, which are the focus of this paper. Numerous formulations for different state based constitutive responses appear in the literature. We identify three formulations of the force density applicable to linear elastic materials:

1. The dilation state-based model proposed in Silling, 2007 [19] with the plane-strain modification found in Le, 2014 [22] and Ouchi, 2015 [18].
2. The deformation gradient-based model proposed in Silling, 2007 [19].
3. The dilation state-based model proposed in Oterkus, 2012 [23].

In this study, we investigate and compare each of these three methods.

In addition to the choice of force density law, an important issue is the selection in the peridynamic influence function, $w(r)$. This function is used to weight the calculations of the force densities and states by the distance between two material points. The selection is arbitrary with respect to the physical theory, but the impact of this selection not yet been studied in the literature in the context of discretization refinement. A number of different expressions have appeared in the literature. A common choice is a piecewise constant influence function that is finite inside the horizon and vanishes outside [19] (this can be considered the default case when a force density law makes no mention of the influence function). Oterkus, 2012 used an inverse radial law that was truncated at the horizon limit to parameterize the given force density law [23]. Bobaru, 2008 compared constant, decreasing-with-distance linear, and increasing-with-distance linear influence functions for a 1D elastic bar, determining that all would give correct results, but the increasing-with-distance was numerically ill-conditioned [24]. Bobaru, 2011 compared the constant function with a linear-cone function in 2D analysis with the bond-based force density, concluding that the conical function produces smaller boundary effects [25]. The effect of the influence function's support size on crack propagation was studied in Bobaru, 2012, which concluded that the effect on crack behavior was due to wave dispersion properties and that the horizon size has no effect when stress–wave interaction does not play a roll in the problem setup [26]. Seleson, 2011 varied the exponent influence functions of the form $1/r^p$ to characterize the effect on dispersion in elastic wave propagation for a fixed grid size in 1D and 3D bond-based models, concluding that the accuracy of the model increases as the exponent p increases [9]. Because Seleson, 2011 only examines one discretization and

support radius size, the refinement of increasing p is equivalent to showing that peridynamics converges as the horizon shrinks by assigning very small weights to farther particles, and does not draw any conclusions about the influence function itself. In our analysis, we focus on evaluating and comparing the accuracy of the aforementioned peridynamic force density laws using different forms of the influence function. To accomplish this, we extend the model of Oterkus [23] to handle arbitrary influence functions. We use the analytical solutions for four simple test problems from linear static mechanics to evaluate the accuracy of the numerical solutions. We focus on studying the spatial discretization produced by the peridynamic representation. We do not consider dynamic behavior or damage evolution, but these will depend on the spatial discretization themselves. We determine the convergence rate for the different models by separately varying the grid point discretization and the relative horizon size. It is a standard criterion that a numerical code should be able to reproduce the correct results for these simple problems with a well defined convergence trend during refinement. Otherwise, no verification or benchmarking of the code is possible, rendering it unsuitable for practical engineering analysis.

Section 2 describes the peridynamics theoretical framework and the three different peridynamic models used. Section 3 describes the numerical discretization of the peridynamics equations and procedure for performing the local integration.

Section 4 describes the code implementation and lists the supporting libraries used. Four model problems with known analytical solutions are used as test cases. The first three problems represent independent linear deformation modes and are discussed in Section 5, in which the application is every combination of force density law and influence functions. In Section 6, a crack filled with a pressurized fluid embedded in an infinite elastic domain is solved using a subset of the best-performing methods.

Section 7 summarizes the conclusions from the studies and proposes future direction for development of the peridynamics theory. The process of determining and generating the tangent matrix for arbitrary peridynamic constitutive responses is discussed in the Appendix.

2. Peridynamics

2.1. Overview

In the peridynamics theory, each material point in the body, at $\mathbf{x}$, is dependent via an integral relation on the other material points within a compact horizon, $H\mathbf{x}$. The reference position of the material point is $\mathbf{x}$, and its current deformed position is $\mathbf{y}$. In the horizon integrals, $\mathbf{x}'$ and $\mathbf{y}'$ denote the reference and current positions of another point in the

horizon of x. The connection between points x and x' is referred to as the bond between the points, denoted by ξ. With peridynamic fields and states, the notation $a\langle x\rangle$ denotes that a is a function of a material point x, and the notation $b\langle x,\xi\rangle$ denotes that b is a function of the bond ξ at point x. The arguments will often be dropped in the following equations without ambiguity for conciseness. The distance vector between reference positions is denoted by $\xi = x' - x$, and the distance vector between deformed locations is denoted by $Y\langle x,\xi\rangle = y' - y$. The deformation states are illustrated in Fig. 2.

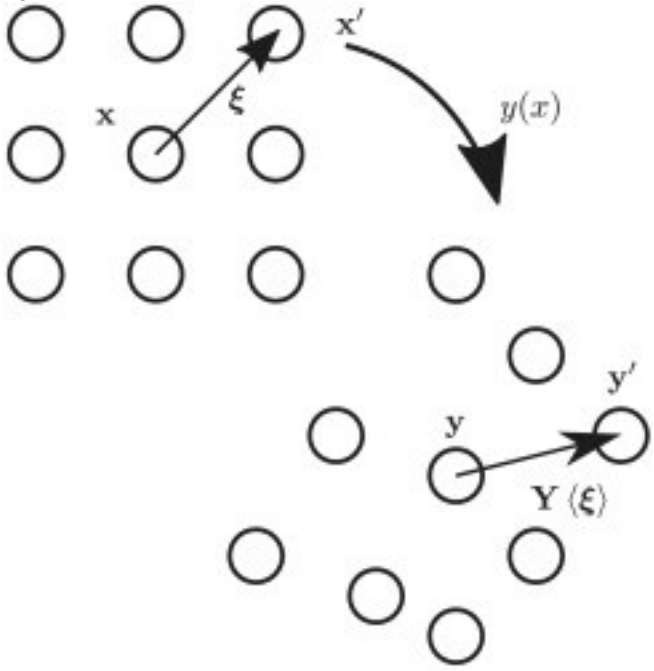

1. Download high-res image (120KB)
2. Download full-size image

Fig. 2. Deformation of a set of peridynamic material points.

The dynamic balance of linear momentum for peridynamics follows the second order ordinary differential equation

$$\rho\ddot{y} = \int_{H_x} t\langle x, x'\rangle\langle \xi\rangle - t\langle x', x\rangle\langle -\xi\rangle \, dV_{x'} + \rho b\langle x\rangle \quad \forall x \in \Omega \tag{1}$$

where ρ is the material density, t is the peridynamic force density, and b is a body force [1], [19], [27]. For the static or quasistatic approximation, the above equation is solved as an implicit equation with $\dot{y} = \ddot{y} = 0$. The integral for the state-based force density contains contributions from “both sides” of the bond, using the states at x to compute $t\langle x\rangle$ using the points in the horizon H_x, and the states at x' to compute $t\langle x'\rangle$ using the points in the horizon $H_{x'}$, as illustrated in Fig. 3.

The quantity $t\langle x,\xi\rangle$ is the peridynamic force density, and its specification is the peridynamic constitutive response for the material. There are various ways to express the material

responses. The parameters of a given force density law are typically determined by comparing a test deformation to the known solution from mechanics [19], [23]. The traditional bond-based peridynamics model calculates force densities using two particles at a time, which is very simple to implement but has the limitation of only capturing isotropic materials with a Poisson ratio equal to 14 in 3D or 13 in 2D [23]. In state-based models, the deformation states of all particles within the horizon (see Fig. 1) are used to calculate $\underline{t}\langle x, \xi\rangle$. The theoretical requirements on the expressions to satisfy balance of linear momentum, balance of angular momentum, etc., are thoroughly discussed in Silling, 2007 [19]. In the following sections, we describe three different choices of the material response $\underline{t}$ that are each based on different state calculations. A key component in each of these laws is the choice of the peridynamic influence function, w_r. Possible expressions for this function are studied in detail in Section 5; for the discussion in this section it is left as a free selection. A special peridynamic quantity is the bond damage, $\alpha\langle x, \xi\rangle$, that represents material strength and damage at a point x relative to the point x'. The effect of damage is often wrapped into the influence function. In order to clarify experimentations with weighting expressions, the combined result is split into two functions for our discussions, i.e. $\hat{w} = w\alpha$, where w is only the radius-dependent weight function, and α is only the material damage. The damage field weights the force density and state calculations to incorporate the change in connectivity within the material caused by internal failures and cracks. We use the scaling choice wherein $\alpha = 1$ is an undamaged bond and $\alpha = 0$ is a broken bond. Evolution laws for α are used to model fracture and plasticity behavior, but are outside of the scope of this work. For brevity in the following equations, the arguments of w and α are omitted, such that $w\alpha$ is written to imply the product of influence function and bond damage state evaluated at a bond, $w|\xi|\alpha\langle x, \xi\rangle$.

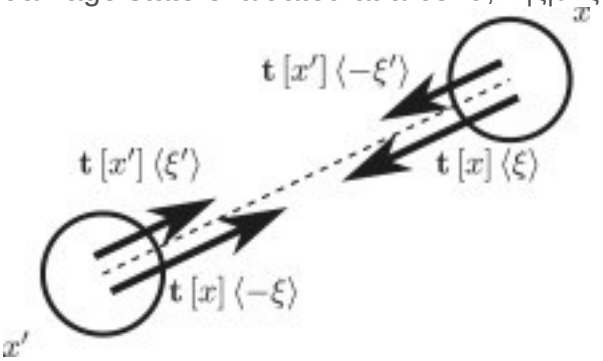

1. Download high-res image (87KB)
2. Download full-size image

Fig. 3. Two pairs of force densities acting on two material points. Each pair of force densities is evaluated based on the state at one of the points and applied with an equal-and-opposite force density on the other.

2.2. Silling's dilation-based method

The linear elastic isotropic model in Silling, 2007 is based upon estimating the dilation at a material point [19]. Firstly, the peridynamics weight scalar m at a point is independent of the material deformation and properties, but depends on the discretization, material connectivity, and choice of influence function, and is calculated by

$$(2) m=\int_H w_\alpha |\xi|^2 d^3x'.$$

This weight scalar is used to properly weight the force density calculations to account for the scale of the influence function and the size of the horizon. The dilation state θ at a point is calculated by performing the integral

$$(3) \theta=\frac{3}{m}\int_H w_\alpha |\xi||Y|-|\xi| d^3x'$$

over the horizon and is a measure of the volumetric strain, related to the continuum linear strain ε by $\theta=3\mathrm{tr}\varepsilon$. After calculating the dilation θ at a point, the force density law is then calculated by

$$(4) t_{x\xi}=w_\alpha m\left(3K\theta\frac{|\xi|}{|\xi|}+15G\left(|Y|-|\xi|\right)\frac{Y}{|Y|}\right)$$

where K is the bulk modulus and G is the shear modulus.

For plane-strain, the parameterization of constitutive response must be changed. Ouchi proposed the following modifications [18] :

$$(5) m=\int_H 2D w_\alpha |\xi|^2 d^2x'.$$

$$(6) \theta=\frac{2}{m}\int_H 2D w_\alpha |\xi||Y|-|\xi| d^2x'$$

$$(7) t_{x\xi}=w_\alpha m\left(2K\theta\frac{|\xi|}{|\xi|}+8G\left(|Y|-|\xi|\right)\frac{Y}{|Y|}\right).$$

Le, 2014 derived the same parameterization for plane strain, albeit written slightly differently [22].[1]

2.3. Oterkus's dilation-based method

Oterkus, 2012 presented a different constitutive response that is also based on estimating the local dilation [23]. The material parameters for this law are a, b, and d. The dilation is instead calculated by the expression

$$(8) \theta=d\int_H w_\alpha |Y|-|\xi|\frac{Y}{|Y|}\cdot\frac{\xi}{|\xi|} dn x'$$

and the force density at each bond is determined by

$$(9) t_{x\xi}=2w_\alpha a d\frac{Y}{|Y|}\cdot\frac{\xi}{|\xi|}\theta+b\left(|Y|-|\xi|\right)\frac{Y}{|Y|}.$$

The strain energy for the above force density law is

$$(10) W=a\theta^2+b\int_H w_\alpha |Y|-|\xi|^2 dn x'.$$

In Oterkus, 2012, these parameters are determined by selecting $w=\delta|\xi|$ and matching local strain energies in isotropic deformation and simple shear deformation with the continuum mechanics strain energies. Here, we generalize the process for any choice of influence function that also includes the surface correction factors for the plane strain case.

Let s denote the scalar parameter of an arbitrary test strain. For the isotropic deformation, the deformation field is $Y=1+s\xi$ for a given s. We require in plane strain that $\theta=2s$ and $W=2Ks2$ for this deformation to match continuum mechanics for all values of s. Substituting this requirement into Eq. (8),

(11) $$2s=d\int_H w\alpha 1+s|\xi|-|\xi|1+s\xi 1+s|\xi|\cdot\xi|\xi|d2x'$$

must hold for all s, so we determine

(12) $$d=2\int_H w\alpha|\xi|d2x'.$$

The strain energy provides the following relation for a and b:

(13) $$2K=4a+b\int_H w|\xi|2d2x'.$$

For simple shear, the trial deformation state field is represented by

(14) $$Y=1s0010001\xi=I+sA\xi$$

where A is the matrix characterizing the shear component with $A12=1$, $Aij=0$ otherwise. The dilation is zero because the motion is isochoric. Let $n=\xi|\xi|$. Analyzing the strain energy density, we require

(15) $$G2s2=b\int_H w\alpha|Y|-|\xi|2d2x'=b\int_H w\alpha snTAn|\xi|2d2x'\forall s$$

which, after substitution of the value from A in Eq. (14), is reduced to the requirement

(16) $$b=G2\int_H w\alpha\xi 1\xi 2d2x'.$$

Combining this result for b with the strain–energy law, the requirement on a is

(17) $$a=12K-2G\int_H w\alpha|\xi|2d2x'\int_H w\alpha\xi 1\xi 2d2x'.$$

This is similar to the result of Oterkus, $a=12K-2G$. The integrals $\int_H w\alpha|\xi|2d2x'$ and $\int_H w\alpha\xi 1\xi 2d2x'$ are calculated discretely at every point when the force densities are calculated.

2.4. Silling's deformation gradient-based method

The final constitutive law we considered is also due to Silling, 2007 and is the closest to traditional continuum mechanics [19]. The deformation gradient is reconstructed from the peridynamics deformation and the stress tensor is related to the peridynamic force densities, allowing classical continuum constitutive responses to be applied. This treatment can be shown to be equivalent to a limiting case of the reproducing kernel particle method [28]. The shape tensor K for the reference configuration at a point is determined by integrating around the horizon,

(18)K=∫Hwαξ⊗ξdnx′.

The deformed shape tensor N is integrated similarly using the deformed bond vector on the left side,

(19)N=∫HwαY⊗ξdnx′.

The deformation gradient F at the point x with a given horizon is calculated from these two matrices by

(20)F=NK−1.

Consequently, the deformation gradient depends on all of the points in the horizon. Using F, the stress can be computed by any constitutive law, e.g. σ=σ^F,p,… for the linear stress. The representation is valid for any nonlinear material response, but we use the linear elastic constitutive law,

σ=K−23Gtrε+2Gε

with ε=12F+FT as the linear strain. From this, the corresponding peridynamic force state centered at the point in the direction of a bond is computed by

(21)txξ=wασK−1ξ.

2.5. Application of boundary conditions

Dirichlet boundary conditions are effected through modification of the linear system of equations, discussed in the next section. Traction boundary conditions are applied by converting the traction, T, into a force density to apply to boundary nodes, i.e.

(22)ρbxB=TApBVpB

where ApB is the area of particle B (or linear-length in 2D) along the face and VpB is the total volume (or area in 2D) of the particle B. The particle side area is calculated for a 2D system with a load on the top by ApB=WNpx, where W is the width of the domain and Npx is the number of particles spaced evenly along the side.

2.6. Fracture pressure on broken bonds

Internal discontinuities are handled by the damage field, αξ that exists on the peridynamic bonds. To produce a crack, the damage field is set to 0 on bonds that cross the crack, as illustrated in Fig. 4. The above expressions for tξ will not depend on a broken bond and will not produce a force for a broken bond, when αξ=0. The impetus for this study and our interest in this work is to develop a model for the initiation and evolution of hydraulic fracture in the subsurface. The following law is used, which depends on the fracture pressure at the bond:

(23)txξ=pf2dV|Y|Y|Y|ifαξ=0.

The fracture pressure is only applied to bonds between adjacent particles, so that it effectively becomes an internal boundary condition. The factor of 12arises from the fact that at each bond for each particle the total force density is txξ+tx′−ξ′, and the 1dV cancels out the volume of integration in Eq. (1) during the discrete summation process.

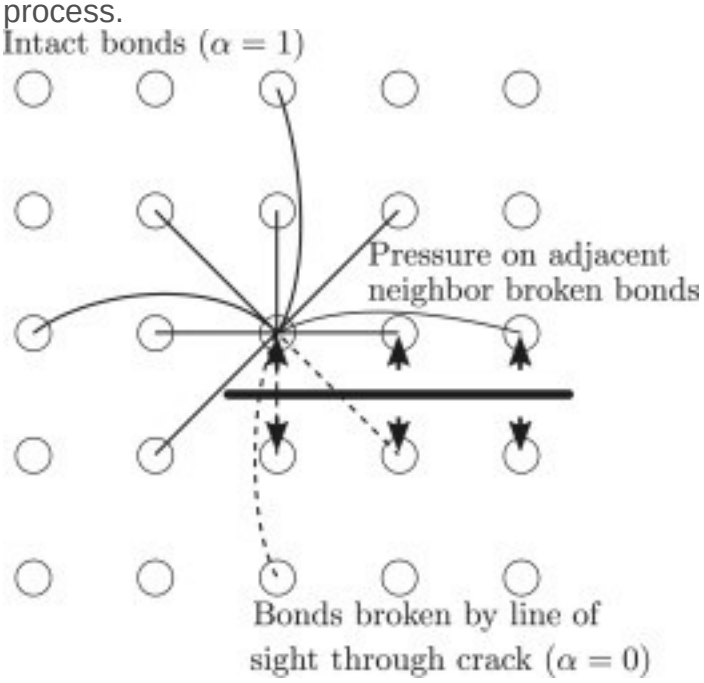

1. Download high-res image (162KB)
2. Download full-size image

Fig. 4. Treatment of bonds near cracks.

3. Discretization of equations

The standard methodology in peridynamics is to perform the calculations in a molecular-dynamics-esque explicit time stepping scheme [2], [8]. Indeed, the widely used code EMU is implemented directly in the LAMMPS molecular dynamics code [8], [29]. For dynamic problems, this is a sufficient approach. Artificial dampening methods are used to solve static problems, such as the adaptive dynamic relaxation method [10].
This work alternatively solves the system of equations arising from the static force balance by solving a tangent stiffness matrix. This approach is not common but is not unique to this work: Bobaru, 2008 obtained solutions to the peridynamic balance of momentum by solving a matrix for a 1D problem [24], and the open-source code Peridigm uses both explicit and implicit time stepping using numerical differentiation to compute the tangent stiffnesses [30], [31]. In our implementation, a custom written package for automated symbolic differentiation is used to generate the code for the load

vector and consistent tangent matrix calculations for arbitrary peridynamic force density expressions.

Let $\sum_{A \in H}$ denote the summation of all points indexed by A within the horizon of the current material point being evaluated. The peridynamic horizon integrals are evaluated with center point integration by summing over all of the discrete points in the horizon and multiplying by the particle volumes V_A (or areas in 2D). The discrete equations for the intermediate values needed by Silling's dilation-based response, Eqs. (5), (6), are, respectively,

$$m = \sum_{A \in H} w_\alpha |\xi_A|^2 V_A \tag{24}$$

$$\theta = \frac{3}{m} \sum_{A \in H} w |\xi_A| (|Y_A| - |\xi_A|) V_A. \tag{25}$$

The summation needed for the integral in the numerator of d in Oterkus's method, Eq. (12), is identical to the summation for m. The additional summation needed for Oterkus's method to calculate the denominator shared by b and a in Eqs. (16), (17) is

$$\int_{H} w_\alpha \xi_1 \xi_2 dx' = \sum_{A \in H} w_\alpha \xi_{1,A} \xi_{2,A} V_A. \tag{26}$$

The deformation gradient-based force density requires two summations for the tensors K and N, Eqs. (18), (19), which are

$$K = \sum_{A \in H} w_\alpha \xi_A \otimes \xi_A V_A \tag{27}$$

$$N = \sum_{A \in H} w_\alpha Y_A \otimes \xi_A V_A \tag{28}$$

in which each loop computes a contribution to each component of a 2-by-2 matrix.

The peridynamic force density integral is also performed by using a center-point integration summation. The discrete equations of motion for a given material point B are obtained by adding the body force density (or converted boundary traction) at the material point to the sum of the force densities with each point in the horizon:

$$\rho \ddot{y}_B = \rho b_{x_B} \underbrace{\text{Body force/BC}}_{} + \sum_{A \in H} t_{x_B x_B - x_A} V_A \underbrace{\text{Force from this state}}_{} - t_{x_A x_A - x_B} V_B \underbrace{\text{Force from neighbor's state}}_{}. \tag{29}$$

At each point x_B, two force densities are summed for each pair, one due to the state at x_B and the other due to the state at x_A. The discrete integration of Eq. (23) cancels out the volume of integration, so that

$$t_{x_B \xi} V_A = p f_{x_B \xi} \frac{2|y_B - y_A|}{|y_B - y_A|} \text{ if } \alpha_\xi = 0 \tag{30}$$

resulting in the point-wise application of a boundary traction.

The displacements of every peridynamic particle are solved by assembling a linear system from the discretized of balance of momentum equations,

$$Ku = R \tag{31}$$

where R is a vector stacking the total force densities at each material point, u is a stack of displacements at each material point, and K is the global tangent (or stiffness) matrix

satisfying $K=\partial R\partial u$. Using the assembly notation in finite element literature, the procedure for assembling the global right-hand-side vector is

(32)$R=\sum A\in HBtxBxB-xAVA-txBxB-xA1VA1\vdots-txBxB-xALVAL$

where N is the total number of particles, $A\in HB$ denotes looping over all particles within the horizon of B, excluding B, and Ai indexes the horizon particles from $A1$ to AL, with L as the number of particles in the horizon. In the same notation, the global matrix is assembled by

(33)$K=\sum A\in HBkA$

where kA is local stiffness matrix contribution obtained by differentiating the local material response. The form of kA is described in the Appendix. The Dirichlet boundary conditions are applied by the standard method of clearing a row and setting the diagonal entry to 1 in the matrix and setting the corresponding row in R to the prescribed value.

The pseudocode in Algorithm 1 describes the calculation of interaction force densities. The main loop is transposed from the apparent implementation suggested by Eq. (29). In this scheme, all of the force densities and state calculations corresponding to a single horizon are performed together and symmetry is exploited to apply the force densities at neighbors. This order of calculations removes unnecessary repeated calculations and

storage and improves memory locality for cache performance.

Algorithm 1 Evaluation of the Peridynamic discrete system of the equations

1. Loop over every particle B:
   (a) Initialize $m = 0$ and $\theta = 0$
   (b) Loop over every particle A in the horizon $\mathcal{H}(\mathbf{x}_B)$:
      i. Add $w\,|\boldsymbol{\xi}_A|^2\,V_A$ to m variable
   (c) Loop over every particle A in the horizon $\mathcal{H}(\mathbf{x}_B)$:
      i. Add $\frac{3}{m} w\,|\boldsymbol{\xi}_A|\,(|\mathbf{Y}_A| - |\boldsymbol{\xi}_A|)\,V_A$ to θ variable
   (d) Loop over every particle A in the horizon $\mathcal{H}(\mathbf{x}_B)$:
      i. Add $-\mathbf{t}[\mathbf{x}_B]\,\langle \mathbf{x}_B - \mathbf{x}_A \rangle\,V_A$ to the force density at A
      ii. Add $\mathbf{t}[\mathbf{x}_B]\,\langle \mathbf{x}_B - \mathbf{x}_A \rangle\,V_A$ to the force density at B
   (e) Compute tangent expressions for $\frac{\partial \theta}{\partial \mathbf{y}_A}$, $\frac{\partial \theta}{\partial \mathbf{y}_B}$, etc.

Algorithm 1 Evaluation of the Peridynamic discrete system of the equations

1. Loop over every particle B:
   (a) Initialize $m = 0$ and $\theta = 0$
   (b) Loop over every particle A in the horizon $\mathcal{H}(\mathbf{x}_B)$:
      i. Add $w\,|\boldsymbol{\xi}_A|^2\,V_A$ to m variable
   (c) Loop over every particle A in the horizon $\mathcal{H}(\mathbf{x}_B)$:
      i. Add $\frac{3}{m} w\,|\boldsymbol{\xi}_A|\,(|\mathbf{Y}_A| - |\boldsymbol{\xi}_A|)\,V_A$ to θ variable
   (d) Loop over every particle A in the horizon $\mathcal{H}(\mathbf{x}_B)$:
      i. Add $-\mathbf{t}[\mathbf{x}_B]\,\langle \mathbf{x}_B - \mathbf{x}_A \rangle\,V_A$ to the force density at A

1. Download high-res image (207KB)
2. Download full-size image

The other two force density laws follow similar procedures, with steps a, b, and c replaced with the appropriate expressions. The deformation gradient-based model is further complicated by the tensor-quality of the states K and N, particularly by the computation of the tangent. The calculation of the tangent matrix for the force densities in steps e and f is discussed in the Appendix.

4. Implementation

The routines for calculating the peridynamic force laws are made using a code generation and symbolic differentiation system implemented using Sympy [32]. The system allows for the specification of peridynamic laws in Python and auto-generates the necessary C code for evaluation of the forces, tangents, and other evaluations. These C routines are compiled and are linked at runtime with hand-written C routines for assembling the global stiffness matrix and load vectors. The main program logic is implemented in Python and is linked to the C library routines using SWIG. The main program executes in serial and is written in Python, with calls to the C library to assemble the finite element and peridynamic integrals. Numpy [33], Scipy [34], and Lis: a Library of Iterative Solvers for Linear Systems [35] are used to perform the linear algebra operations required. The linear systems are solved using Scipy's direct solver for small matrices below 80,000 unknowns and using Lis's Generalized Minimum Residual method (GMRES) solver for larger matrices. Post processing is performed in Python, and plots are produced using Matplotlib [36].

5. Linear compression tests

5.1. Problem description

The peridynamic models are first tested on a set of the simplest problems in static analysis: (1) uniaxial compression, (2) isotropic compression (or, rather, biaxial compression because to the plane strain condition), and (3) simple shear.

The traction T is translated into a force density to be applied to the peridynamic particles along the top edge by

(34)$$ρb_{2,B}=\frac{T}{WN_{edge}V_p}B$$

where W is the width of the domain, N_{edge} is the number of particles along the edge, and V_p is the 2D particle area.

The three test problems are illustrated in Fig. 5. In the uniaxial compression problem, the bottom edge is clamped, both sides have vertical roller boundary conditions, and the top edge is subjected to an applied traction T oriented in the vertical direction. In the isotropic/biaxial problem, the bottom and left edges have roller boundary conditions, and the top and right edges are subjected to applied tractions T in the normal direction. In the simple shear problem, the bottom edge is clamped, the left and right sides are attached to horizontal rollers (allowing motion to the left and right, but not up or down), and the top edge has an applied tangential traction of T. The analytical solution for these problems are:

Table 1. Problem parameters for linear compression tests.

Parameter	Value
Domain dimensions, H **and** W	**10.0 mm**
Young's Modulus, E	1000 GPa
Poisson ratio, ν	0
Load, T	10^{-3}GPa

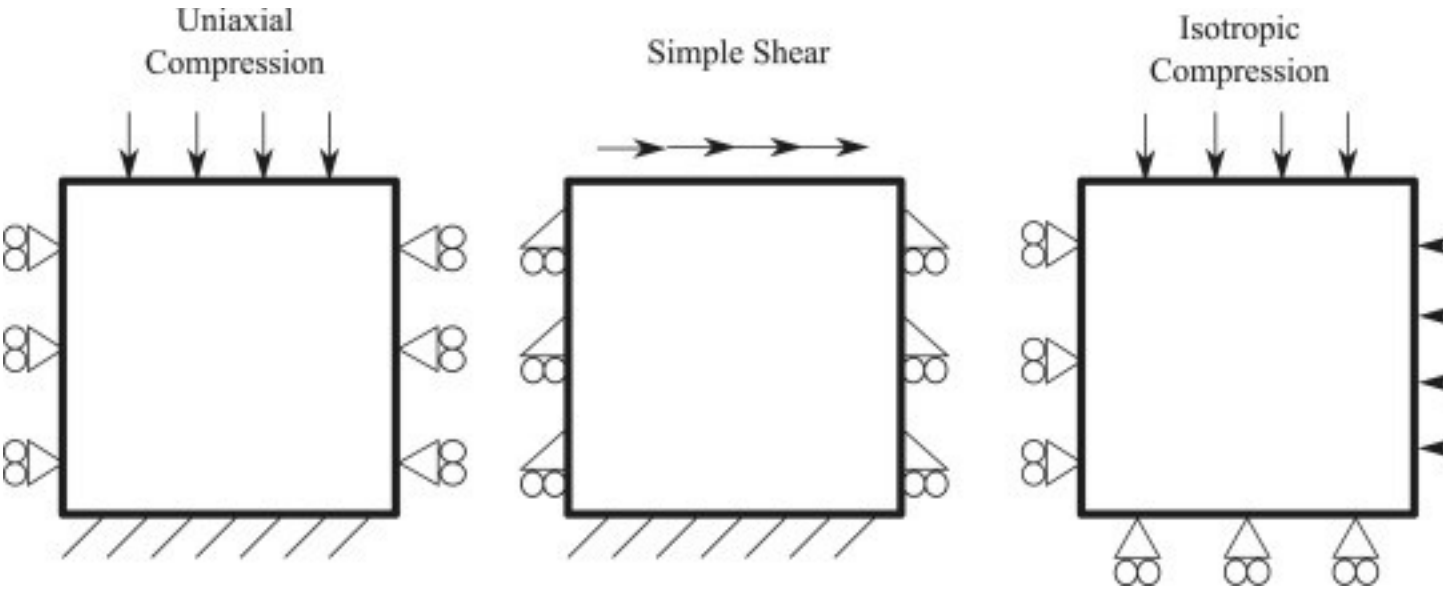

1. Download high-res image (187KB)
2. Download full-size image

Fig. 5. Boundary condition schematics of the three linear test problems.

Test	Solution
Uniaxial	$u_{y,anal} = \frac{TH}{2\nu^2+\nu-1}E(\nu-1)$
Isotropic	$u_{y,anal} = \frac{TH}{1-\nu-2\nu^2}E$
Shear	$u_{x,anal} = \frac{2TH}{1+\nu}E$

The values of the parameters used in for the three simulations are listed in Table 1.

The value of the x- or y- displacement along the top edge of the domain is used to judge to numerical solutions. The displacement fields are probed by averaging the x- or y-displacement of the set of particles near the middle of the edge in the region defined by $y=H$ and $0.4H\leq x\leq 0.6H$, with the averaging equation

$$u_{y,num}=u_y(x)\quad 0.4H\leq x\leq 0.6H \quad and \quad y=H. \tag{35}$$

The same averaging calculation with appropriate exchanges between x- and y-components is used to probe the solutions for the x-displacement along the right edge for the biaxial deformation, and the x-displacement along the top edge for the shear deformation. The error between the analytical solution and the numerical solutions is calculated by

$$e_{num}=|u_{anal}-u_{num}|u_{anal}|. \tag{36}$$

The order of convergence $O(h^m)$ can be calculated from a series of errors $e_{num}(h)$ computed from the solutions u_{num} at different grid spacings h by performing the logarithmically scaled linear regression,

$$\log e_{num}=m\log h+b, \tag{37}$$

where m corresponds to the rate of convergence. The regression package in Scipy is used to determine m.

5.2. Results

We tested all three methods in the solution of the three test problems, using the five influence functions shown in Table 2. All the influence functions vanish outside of the horizon ($w(r)=0$ for $r>\delta$). The support radius and the number of material points in the discretization are varied to test the methods' convergence properties.

The spacing between particles, which decreases as more particles are added, is denoted by h. It is often discussed that δ is held constant as $h\rightarrow 0$ is a convergence criterion. However, performing this type of refinement, the number of particles within each particle's horizon increases quadratically, increasing baseline memory and computation requirements cubically. Such a refinement strategy is thus impractical. Instead, we opt for a refinement approach in which the ratio of the peridynamic horizon to the particle size is held constant as the particle size decreases, i.e.

$$RF=\delta h. \tag{38}$$

This process is consistent with refinement approaches used in studying other numerical methods. This refinement procedure is illustrated in Fig. 6. Note how the number of particles covered by the support of the influence function remains constant as the grid is refined so that baseline memory and computation costs are linear with the number of points in the discretization.

Table 2. Influence functions and their labels.

Name	w(r) **in** H(x)
Const	**1**
Inv	δ⁄r
Linear	1−rδ
Quadr	1−rδ2
Cubic	1−rδ3

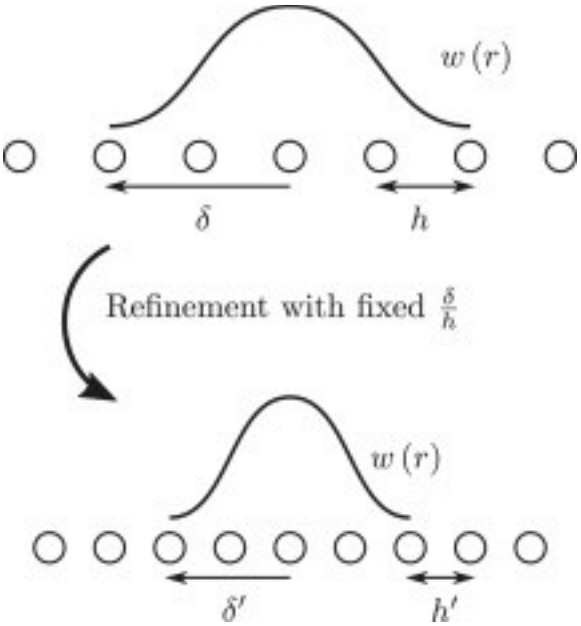

1. Download high-res image (110KB)
2. Download full-size image

Fig. 6. Refinement of the influence function support radius to remain proportional to the grid spacing.

The analytical results along the center vertical axis of the block are shown in Fig. 7. (F is used as shorthand for displacement gradient in the plot labels.) The plots are scaled by the maximum displacement in the analytical solution such that the true solution is a line from the origin to 1.0 at the position of 10 mm. The results are obtained by using 200-by-200 material points in the discretization using a cubic influence function with a relative support radius of 3.5 for the dilation-based models, and both 3.5 and 1.5 for the deformation gradient-based. The plots are zoomed in to the top of the block where the maximum displacement is achieved. The dilation based models are only close to the analytical solutions in one case each. Silling's dilation based model is correct when applied the isotropic deformation problem, and Oterkus's dilation-based model is correct when applied to the shear deformation problem. While the deformation gradient based

model gives the correct result, there is a significant instability with RF=3.5, and a very slight instability with RF=1.5. However, the deformation gradient based model also exhibits an incorrect result in the y displacement on the shear problem where there should be no deformation. The large support radius RF=3.5 has spurious oscillations at a maximum of 4% the magnitude of the x-displacement solution, and the compact support radius has a nonphysical displacement of approximately 0.5%. Both dilation-based models give the correct 0 y-displacement for the shear problem. While the dilation-based models are not accurate in most cases, they do at least give smooth, linear displacement solutions with no spurious features.

The results are grouped by the force density laws in Fig. 8, Fig. 9, Fig. 10. In each figure, the columns denote the problems, and the rows indicate the influence functions. Each subplot shows the logarithmic error with respect to the analytical solutions for five different relative support radii (i.e. varying the relative size of the horizon) as the particle radius decreases.

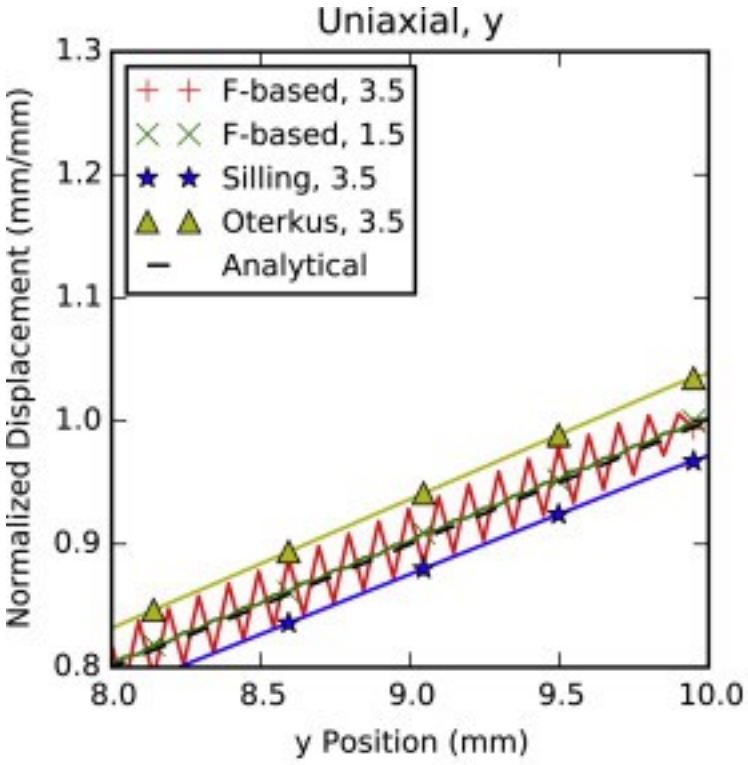

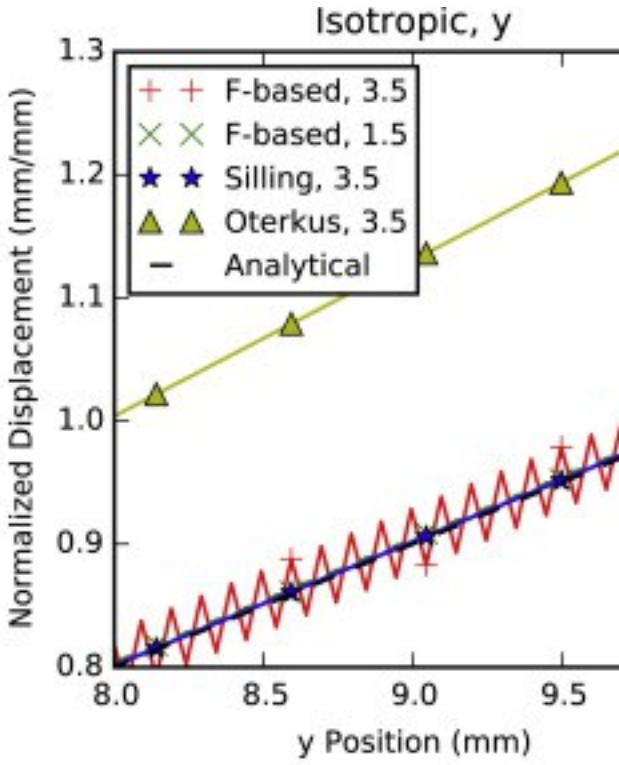

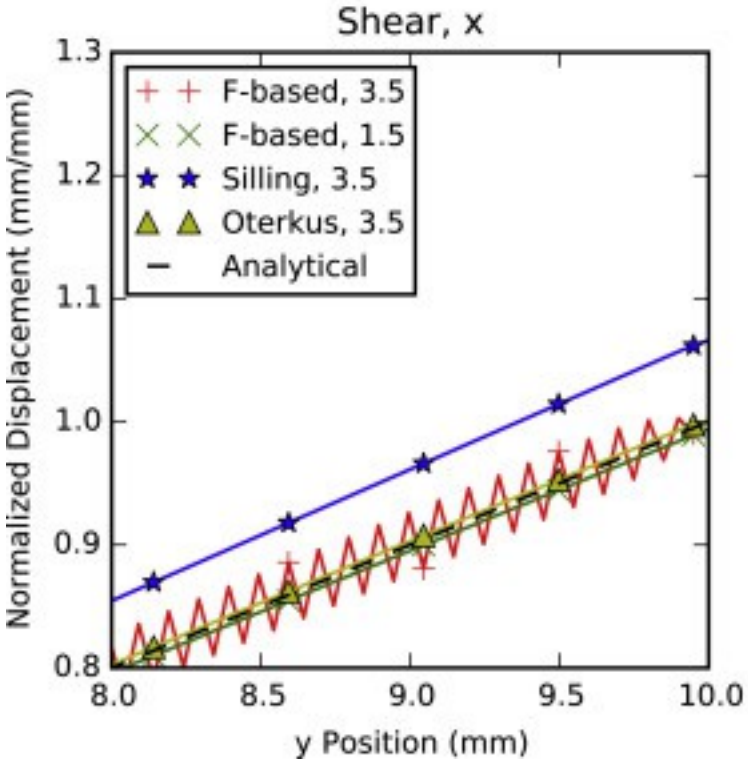

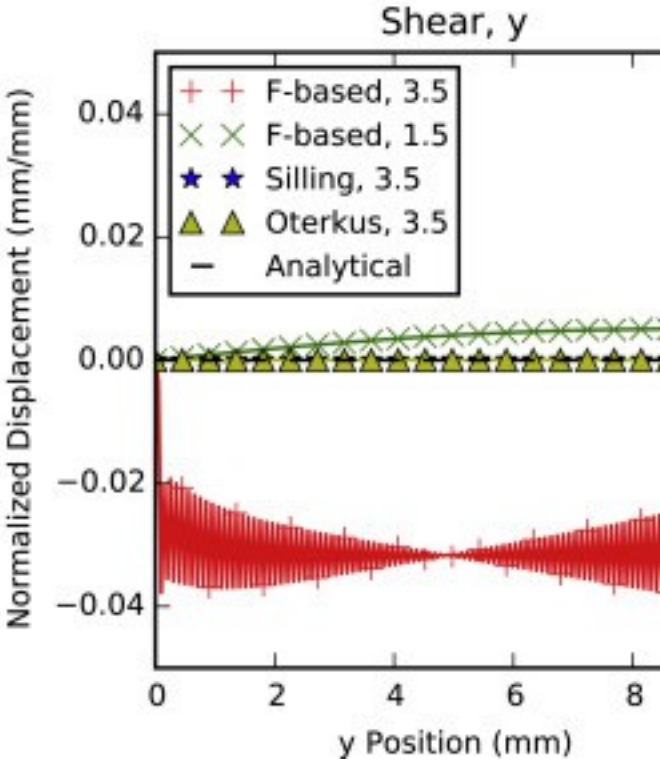

1. Download high-res image (916KB)
2. Download full-size image

Fig. 7. Displacement field solutions along the vertical center axis for the methods using 200-by-200 points, the cubic influence function, and the listed relative horizon size. Displacements are normalized by the analytical solution at the top of the block, where the y-displacement of the shear problem is normalized by the x-displacement solution. Plot markers are only applied to a subset of the data points to improve legibility.

First, let us consider the results associated with the deformation gradient-based force density with results plotted in Fig. 8. The method performs similarly on all three test deformations. The relative support radius $\delta/R=1.5$, which corresponds to the eight nearest points, converges for every choice of influence function. The order of convergence calculated for each influence function (listed in Table 3) indicates that the method achieves $O(h)$ linear convergence in each problem. For large support radii, only the cubic weight function guarantees convergence. Calculating the order of convergence for this function with the different support radii (listed in Table 4), we again observe $O(h)$ convergence for all of the support radii.

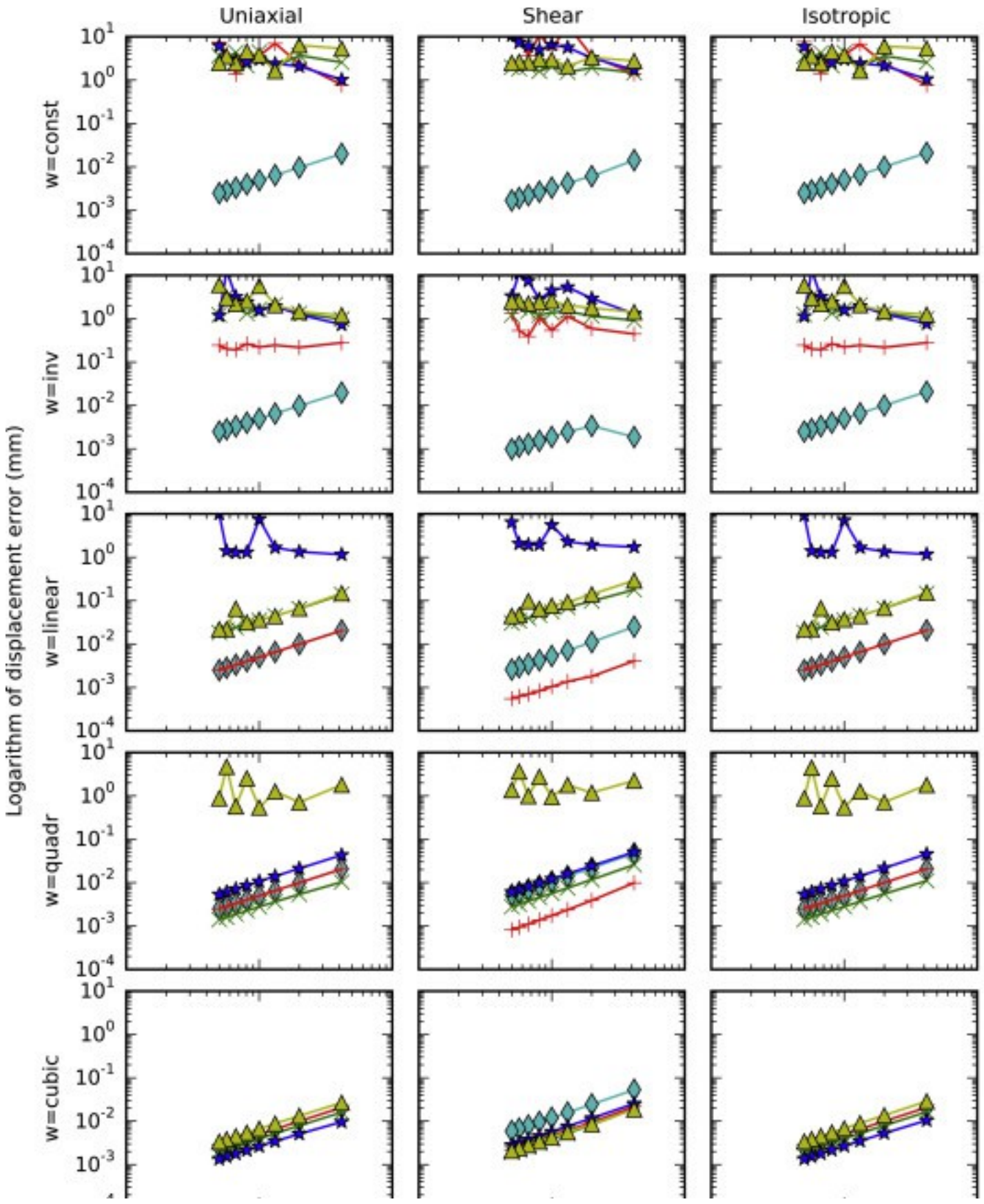
Uniaxial
Shear
Isotropic
w=const
w=inv
w=linear
w=quadr
w=cubic
Logarithm of displacement error (mm)
10^{1}
10^{0}
10^{-1}
10^{-2}
10^{-3}
10^{-4}

1. Download high-res image (1015KB)
2. Download full-size image

Fig. 8. Logarithmic error plots for the deformation gradient based model. Columns show test problem, rows show influence function, and legend key shows relative support radius.

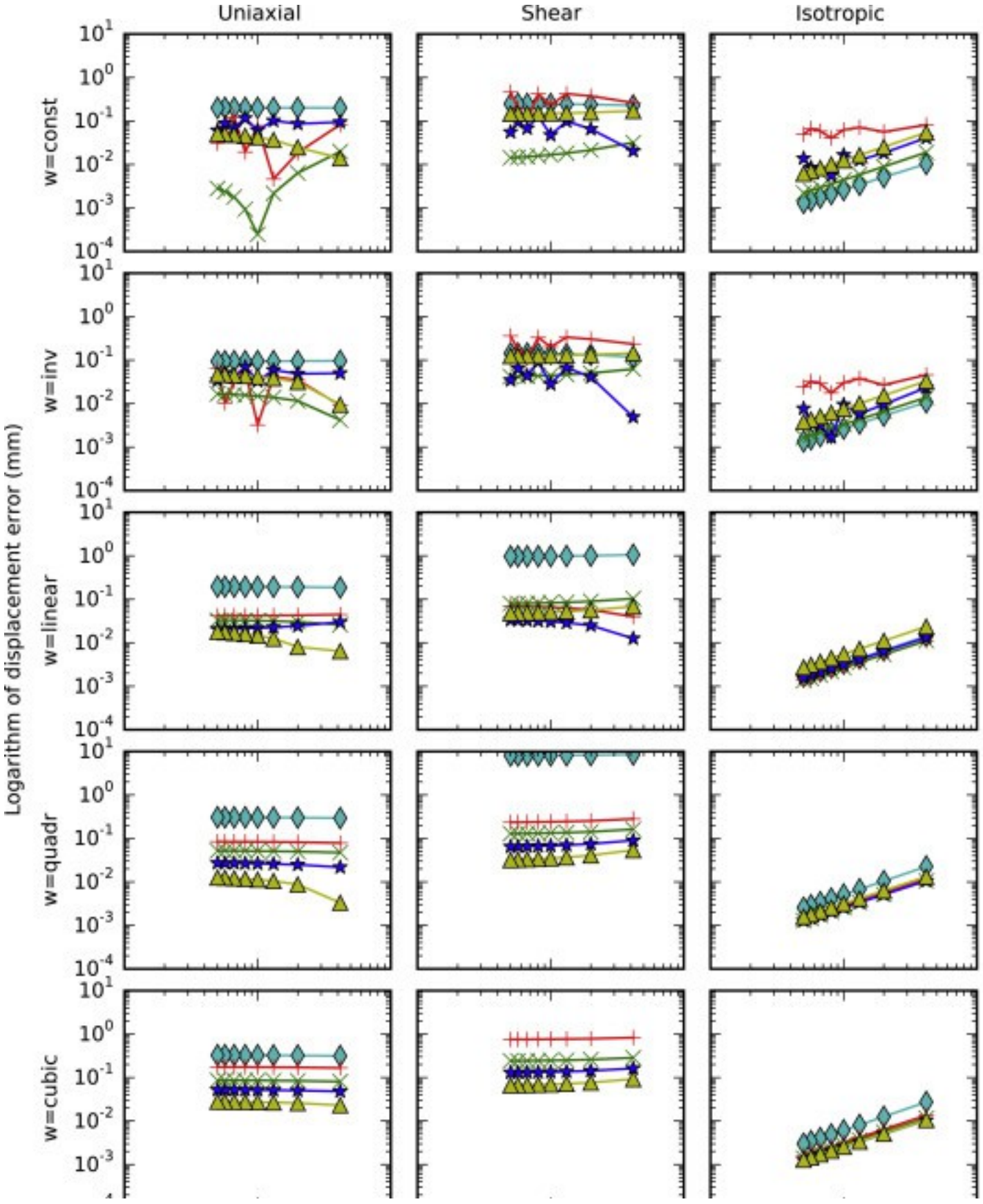
Uniaxial
Shear
Isotropic
w=const
w=inv
w=linear
w=quadr
w=cubic
Logarithm of displacement error (mm)
10^{1}
10^{0}
10^{-1}
10^{-2}
10^{-3}
10^{-4}

1. Download high-res image (1MB)
2. Download full-size image

Fig. 9. Logarithmic error plots for Silling’s dilation state-based model. Columns show test problem, rows show influence function, and legend key shows relative support radius.

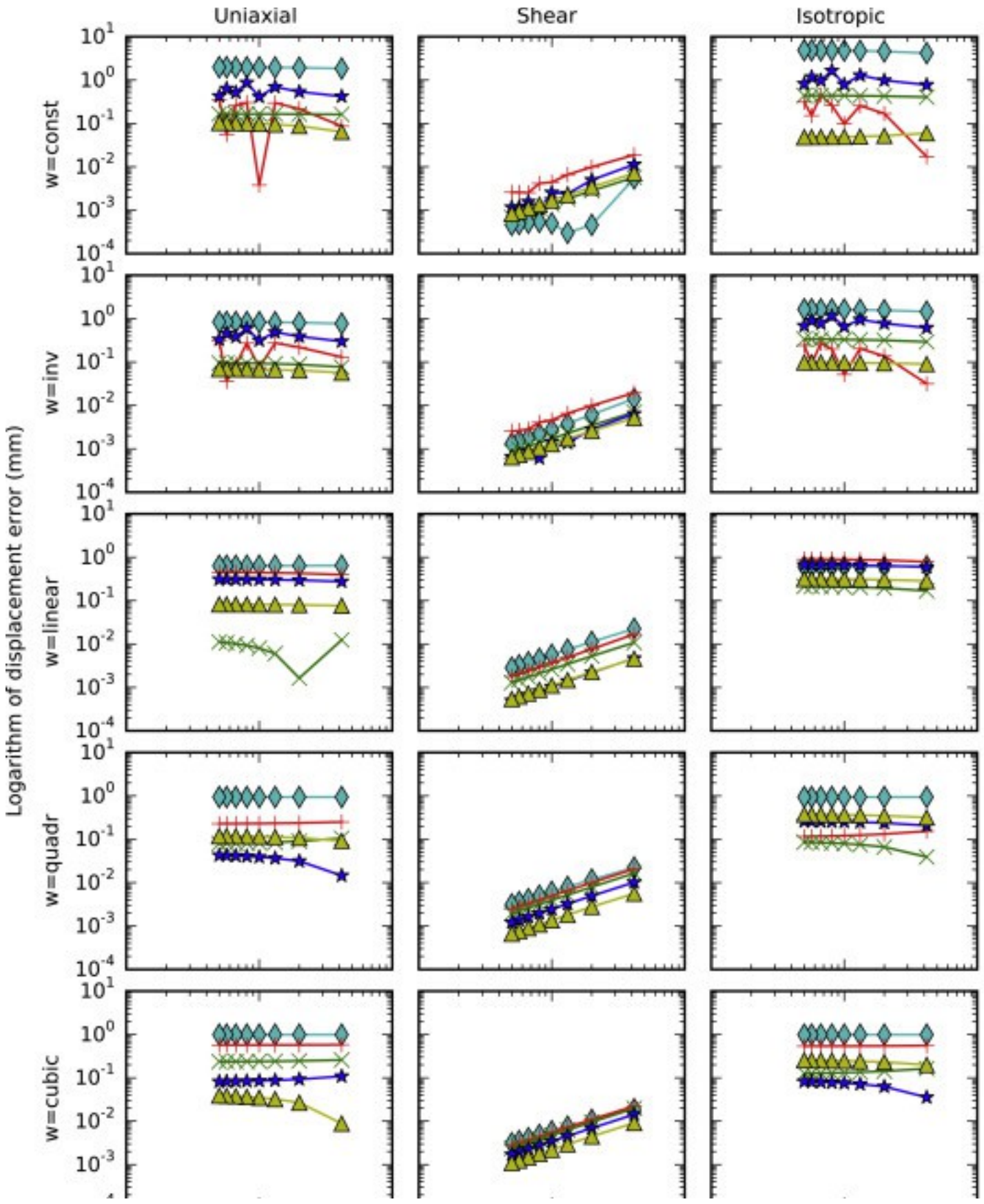
Uniaxial
Shear
Isotropic
w=const
w=inv
w=linear
w=quadr
w=cubic
Logarithm of displacement error (mm)
10^{1}
10^{0}
10^{-1}
10^{-2}
10^{-3}
10^{-4}

1. Download high-res image (1MB)
2. Download full-size image

Fig. 10. Logarithmic error plots for Oterkus's dilation state-based model. Columns show test problem, rows show influence function, and legend key shows relative support radius.

The dilation-based force densities exhibit interesting behavior. The model of Silling only converges in an $h \to 0$ sense for the isotropic compression problem, and the model of Oterkus only converges for the simple shear deformation problem. Only the linear, quadratic, and cubic influence functions guarantee smooth convergence in the two dilation-based methods. The order of convergences for these two methods on the respective isotropic and shear problems is shown in Table 5. In these tests, the two methods achieve linear convergence for all support radii. However, comparison to the other tests leads to the conclusion that these two force density formulations cannot correctly represent every possible constant-strain deformation. That is, the dilation-based methods do not fully span the space of possible independent linear deformations.

Table 3. Order of convergence for the deformation gradient based model with RF=1.5using each influence function.

w(r)	Uniaxial	Shear	Isotropic
Const	**0.9860**	**0.9704**	**1.0005**
Inv	0.9939	0.9247	0.9999
Linear	0.9991	1.0370	0.9996
Quadr	0.9999	1.0192	0.9999
Cubic	0.9999	1.0166	0.9999

Table 4. Order of convergence of the cubic weighted deformation gradient based model as the support radius is varied for each problem.

RF	Uniaxial	Shear	Isotropic
1.5	**0.9999**	**1.0166**	**0.9999**
2.0	0.9988	1.0423	0.9996
2.5	0.9930	1.0423	0.9960
3.0	0.9760	1.0222	0.9875
3.5	0.9922	1.0080	1.0027

Table 5. Order of convergence for the dilation based force density models with the cubic influence function for their respective convergent test problems.

RF	Silling, isotropic	Oterkus, shear
1.5	**1.0227**	**0.9255**

RF	Silling, isotropic	Oterkus, shear
2.0	1.0037	0.9966
2.5	0.9992	1.0075
3.0	0.9976	1.0099
3.5	0.9980	1.0150

6. Linear fracture mechanics results

6.1. Problem set up

Consider an infinite domain with a horizontal crack of length L located at the origin, with a finite equivalent illustrated in Fig. 11. The crack has an internal pressure P acting on the two horizontal faces due to the presence of a pressurized fluid. The idealized domain is infinite with zero displacement towards infinity in all directions,

(39)$$u_x = u_y = 0 \quad \text{as} \quad x^2 + y^2 \to \infty.$$

Likewise, the stress vanishes towards infinity in all directions,

(40)$$\sigma_{xx} = \sigma_{yy} = \sigma_{xy} = 0 \quad \text{as} \quad x^2 + y^2 \to \infty.$$

On the surface of the crack, the stress field has the boundary condition on the normal and shear planes

(41)$$\sigma_{yy} = P, \sigma_{xy} = 0 \quad \text{on} \quad y = 0^+ \text{and} \quad y = 0^- \text{within} \quad x \in -a, a.$$

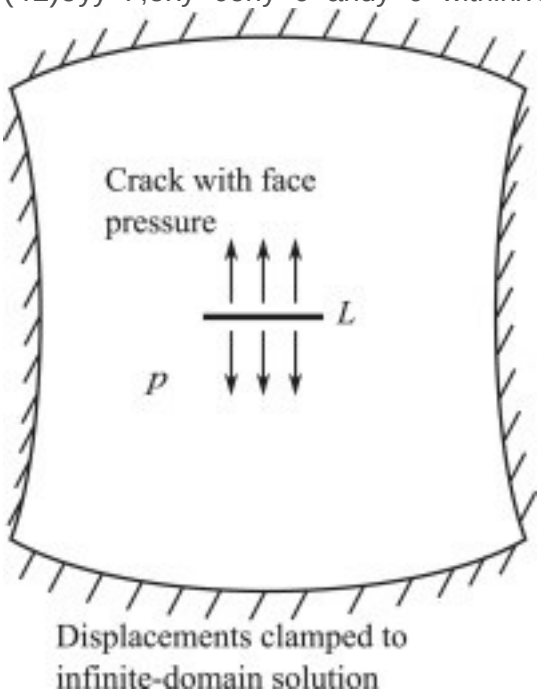

1. Download high-res image (132KB)
2. Download full-size image

Fig. 11. A finite material with a crack with an interfacial pressure. The sides of the finite domain are set to have the displacement field solution matching the infinite domain analytical solution.

Using Westergaard's solution method [37], the complex valued potential function $Z\hat{}$ with the form

(42)$Z\hat{}z=Pz2-L2-z$

with argument $z=x+yi$ satisfies the boundary conditions [38]. This problem has the same solution as if the crack had no internal pressure and instead the material had a far-field tension stress equal to P along the σyy direction. The stress field solution and near-tip displacement solution appear in Sneddon, 1946 [38]. Where $Z=ddzZ\hat{}$ and $Z'=ddzZ$, the stress field solutions are obtained from the potential function by

(43)$\sigma xx=ReZ-yImZ'$

(44)$\sigma yy=ReZ+yImZ'$

(45)$\sigma xy=-ReZ'$

and the displacement field solutions are obtained by

(46)$ux=12G2-4\nu 2ImZ\hat{}-yReZ$

(47)$uy=12G4-4\nu 2ReZ\hat{}-yImZ.$

The analytical solution around the crack is plotted in Fig. 12.

The infinite domain is approximated by a large computational domain satisfying $W\gg L$ and $H\gg L$. To compensate for the finite domain and enable comparison with the analytical solution, Dirichlet boundary conditions are enforced on the x and y displacements matching the analytical solution at the finite distance, as illustrated in Fig. 11. The simulation parameters are listed in Table 6.

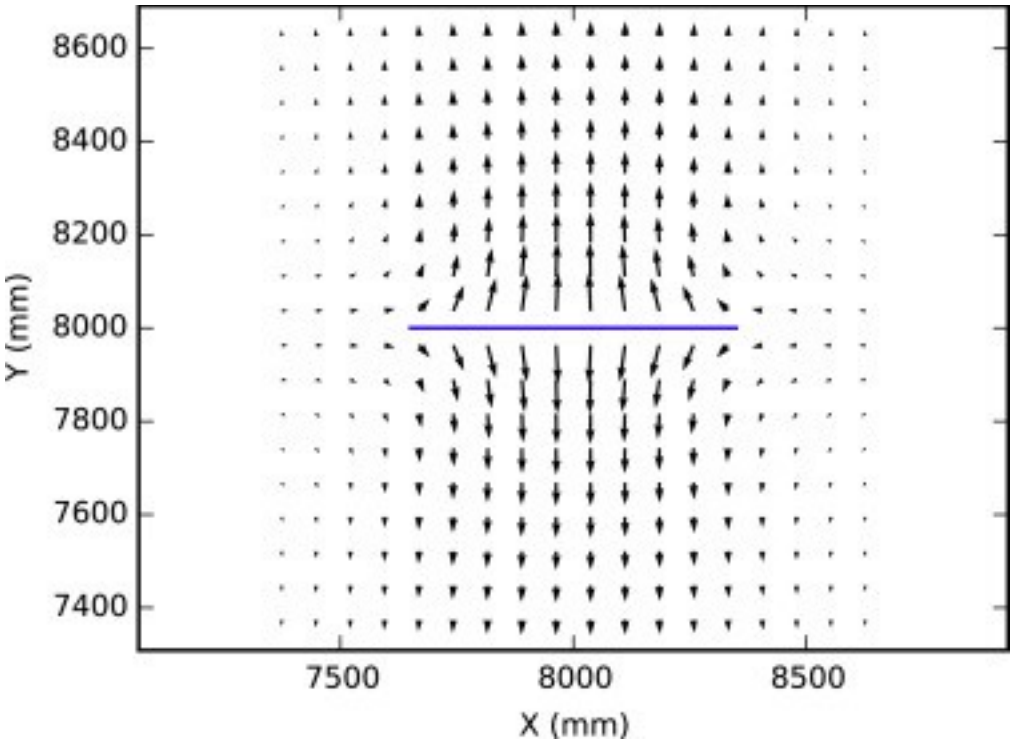

1. Download high-res image (206KB)
2. Download full-size image

Fig. 12. The analytical solution for the displacement in the immediate vicinity around the crack. The crack is draw as a solid line. The displacement vectors are drawn at a 75x scale to the axes.

The crack is included into the peridynamic model by breaking the bonds that intersect the crack, as illustrated in Fig. 4. The damage factor is set to zero at the broken bonds, $\alpha=0$. The bond-pressure is set to the fracture pressure for only bonds that are immediately adjacent. Only an even-number of particles is used to ensure that the crack is always between particles and never exactly on top of a particle.

Table 6. Parameters for fracture simulation.

Parameter	Value
Size H **and** W	160.0×103 **mm**
Young's Modulus E	60 GPa
Poisson's ratio ν	0
Fracture pressure P	0.1 GPa
Fracture length L	700 mm

The integral of the square of the displacement error over the entire domain is used as the error metric, normalized by the magnitude of the integral of the displacement.

Approximating this metric as a summation over the discrete material points, the formula is

(48)$e=\sum_A |u_{anal}x_A - u_{num}x_A|^2 \sum_A |u_{anal}x_A|^2$

where A is the index of the discrete material points, u_{anal} is the analytical solution, x_A are the positions of the material points, and u_{num} is the numerical solution. The volume of the particles cancels out in the above equation because only uniform grids are used.

6.2. Results

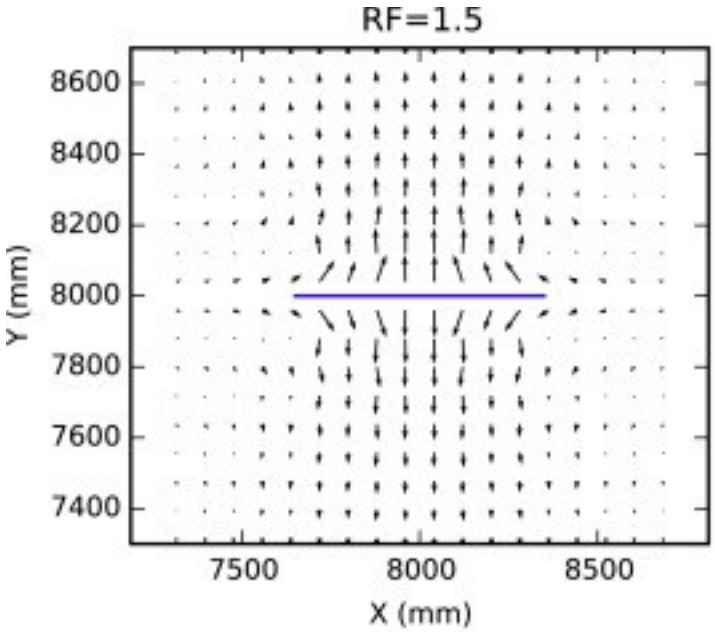
RF=1.5
8600
8400
8200
8000
7800
7600
7400
Y (mm)
7500
8000
8500
X (mm)

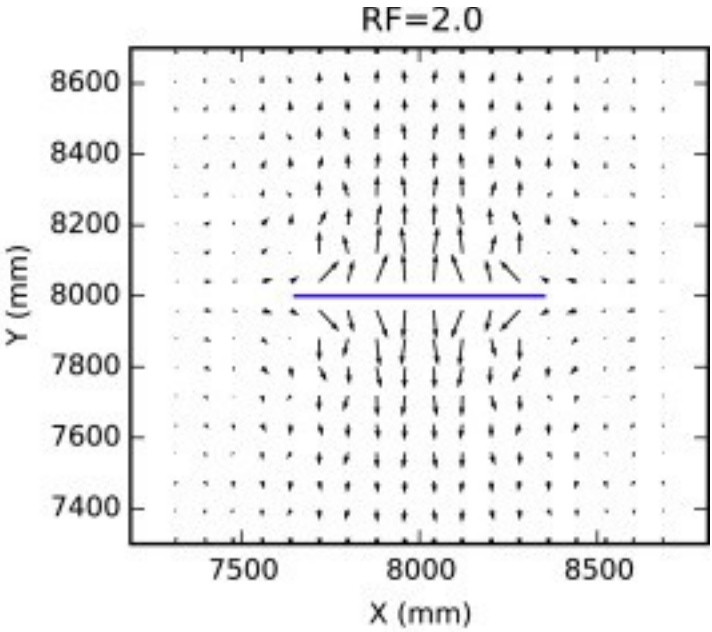
RF=2.0
8600
8400
8200
8000
7800
7600
7400
Y (mm)
7500
8000
8500
X (mm)

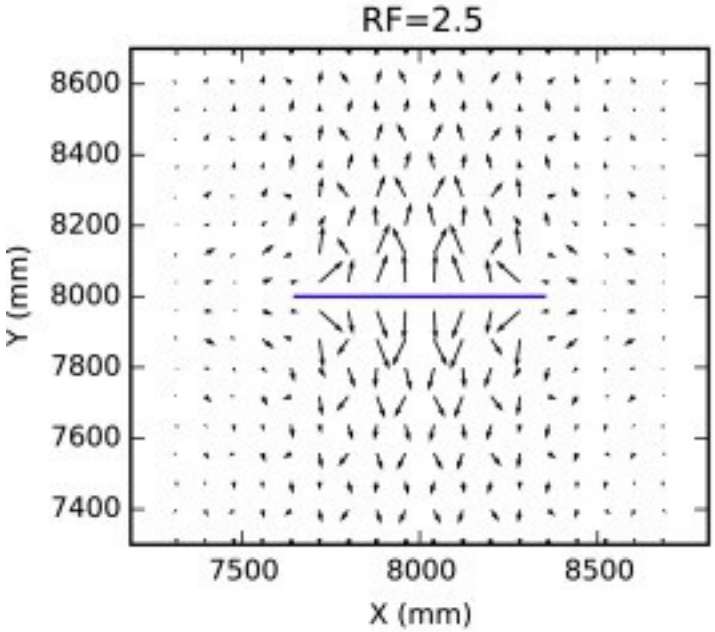
RF=2.5
8600
8400
8200
8000
7800
7600
7400
Y (mm)
7500
8000
8500
X (mm)

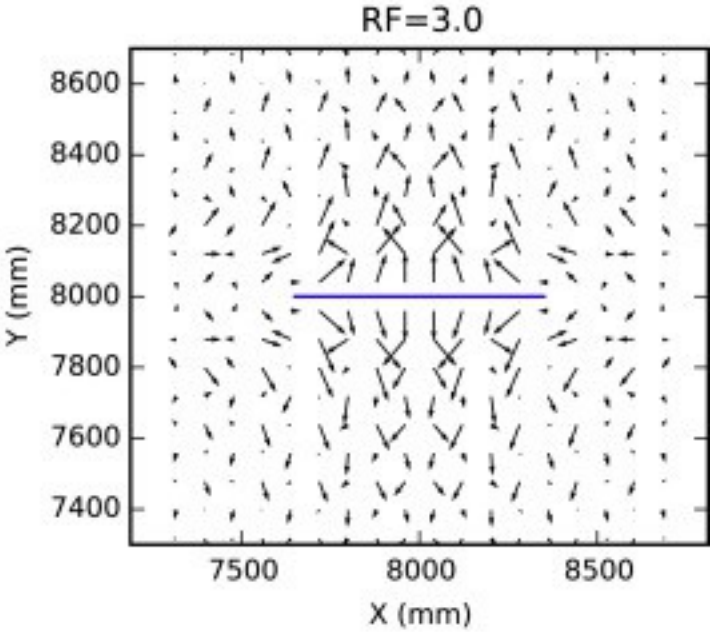
RF=3.0
8600
8400
8200
8000
7800
7600
7400
Y (mm)
7500
8000
8500
X (mm)

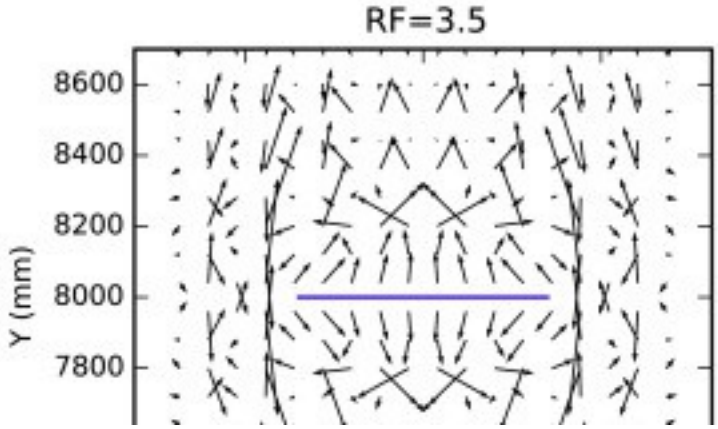
RF=3.5
8600
8400
8200
8000
7800
Y (mm)

1. Download high-res image (807KB)
2. Download full-size image

Fig. 13. Displacement fields for the deformation gradient based solution as the support radius increases near the crack. The scale on the displacement vectors is 75x the scale on the axes.

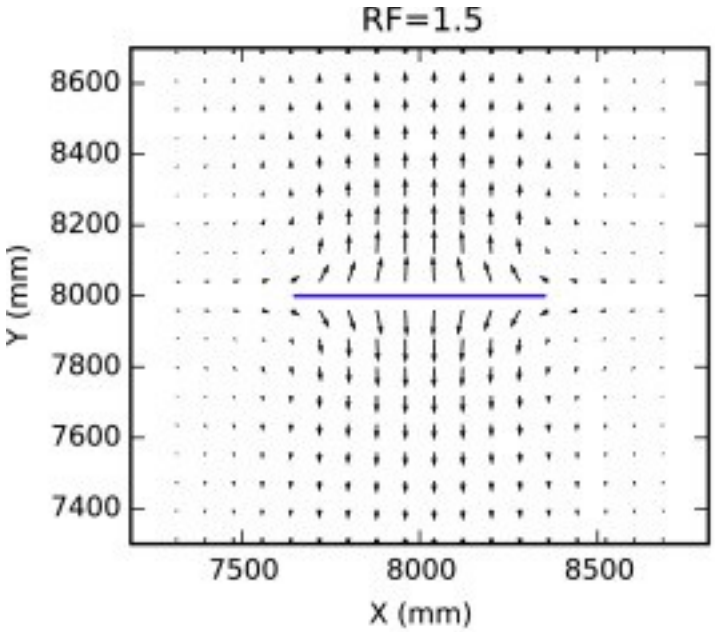
RF=1.5
8600
8400
8200
8000
7800
7600
7400
Y (mm)
7500
8000
8500
X (mm)

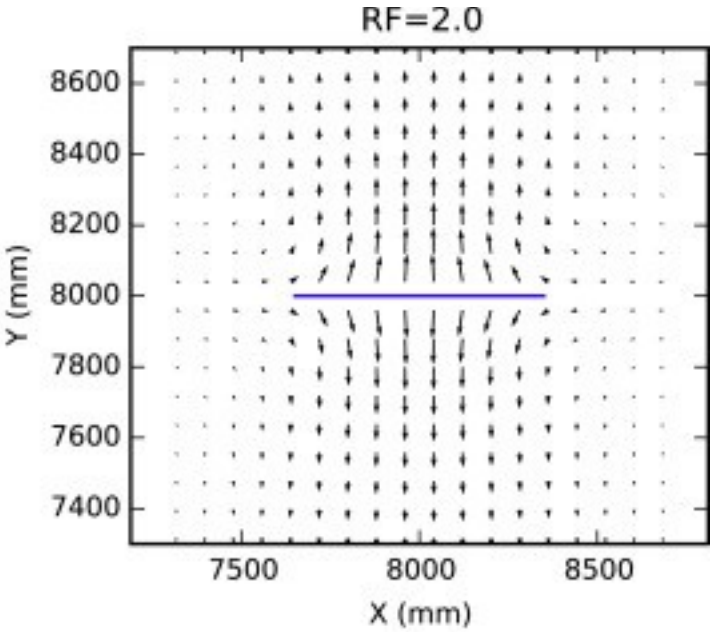
RF=2.0
8600
8400
8200
8000
7800
7600
7400
Y (mm)
7500
8000
8500
X (mm)

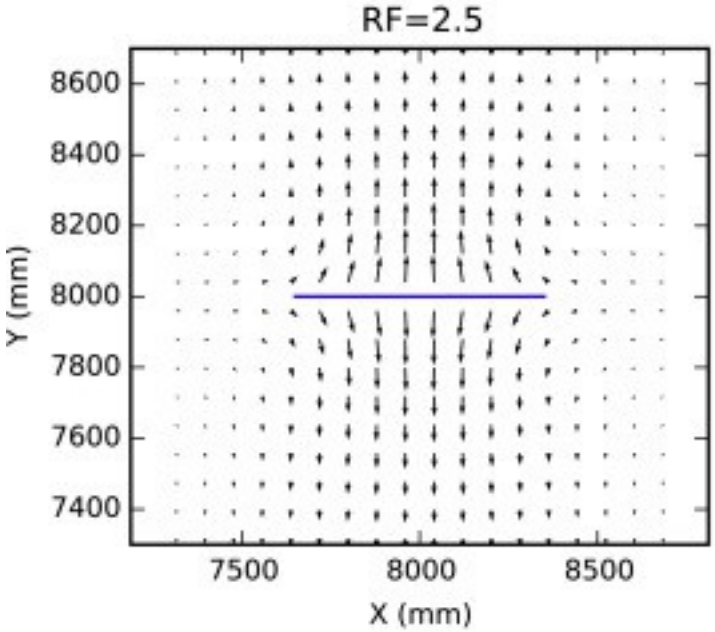
RF=2.5
8600
8400
8200
8000
7800
7600
7400
Y (mm)
7500
8000
8500
X (mm)

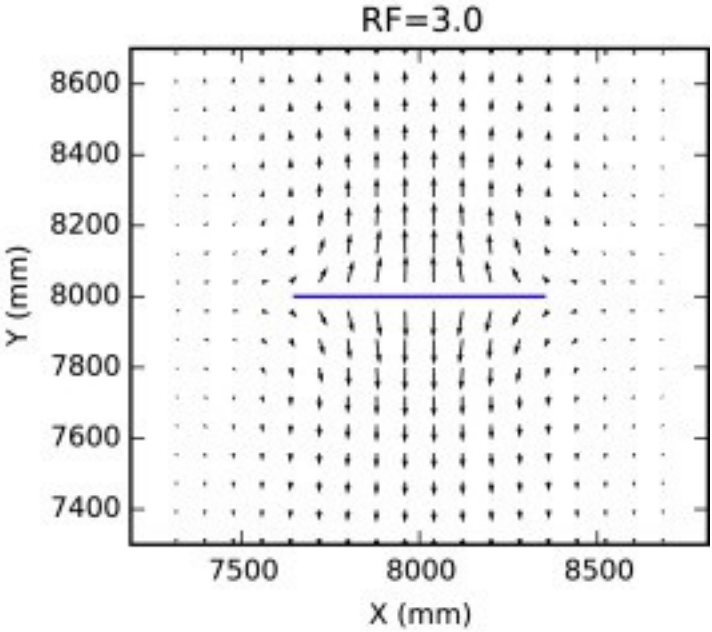
RF=3.0
8600
8400
8200
8000
7800
7600
7400
Y (mm)
7500
8000
8500
X (mm)

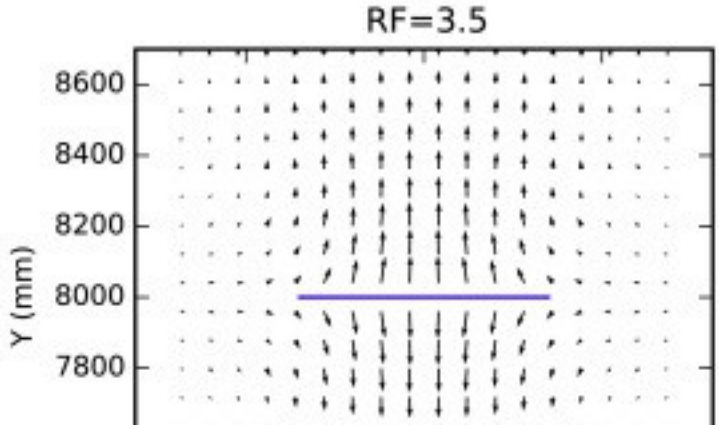
RF=3.5
8600
8400
8200
8000
7800
Y (mm)

1. Download high-res image (711KB)
2. Download full-size image

Fig. 14. Displacement fields for the deformation gradient based solution after a smoothing operation. The scale on the displacement vectors is 75x the scale on the axes.

6.2.1. Instability of deformation gradient model

The deformation gradient force density was solved using the cubic spline influence function. Fig. 13 shows the solved displacement field using this model with 200 by 200 material points in the vicinity of the crack for the various support radius sizes. The displacement vectors oscillate in both the x and ycomponents for each of the radius sizes. As the radius increases, the method becomes increasingly unstable. Without any post processing of the solution, the error increases greatly with increasing support radius, as seen in Table 7. As an ad hoc fix, we experiment by smoothing the solution using the peridynamic influence functions described by the following equation:

(49)usx=∫Hxwx−x′ux′d2x′∫Hxwx−x′d2x′.

Table 7 indicates that the linear influence function gives the smallest error. The displacement fields after smoothing by the linear influence function are plotted in Fig. 14, which confirms qualitatively that the instability is alleviated.

Table 7. Error for different support radii for NP = 200 for the deformation gradient based model for the original solved field and after applying different smoothing operations.

RF	Unsmoothed	Const	Linear	Cubic
1.5	**0.2105**	**0.0836**	**0.0708**	**0.1810**
2.0	0.3022	0.0868	0.0429	0.1697
2.5	0.5409	0.1080	0.0670	0.1628
3.0	1.0375	0.1604	0.1004	0.1965
3.5	2.6741	0.2684	0.1452	0.3302

6.2.2. Convergence as particle size decreases

The two dilation state based models were solved with RF = 3.5 and using the cubic spline influence function. The corresponding displacement fields in the vicinity of the crack for N=200 are plotted in Fig. 15 for both cases. The dilation state based methods do not exhibit the instability problem and qualitatively match the analytical solution.

We examined the following four solutions: the unsmoothed and smoothed deformation gradient based model using a support radius of RF=1.5 and the two dilation state based models using a support radius of RF=3.5. We compared the four sets of solutions to the

analytical solution using the error metric we discussed earlier, and we monitored the error the discretization is refined using the same procedure followed in the previous problems. The refinement is capped at 400-by-400 particles. We note that the dilation state-based models required significantly more computational effort to solve than the deformation gradient-based model with many particles because the support radius RF = 3.5 corresponded to approximately 60 nonzeros per row in the matrix, resulting in a much wider matrix bandwidth. As a result, the 400-by-400 data point is missing for the dilation-based models since the linear system did not converge.

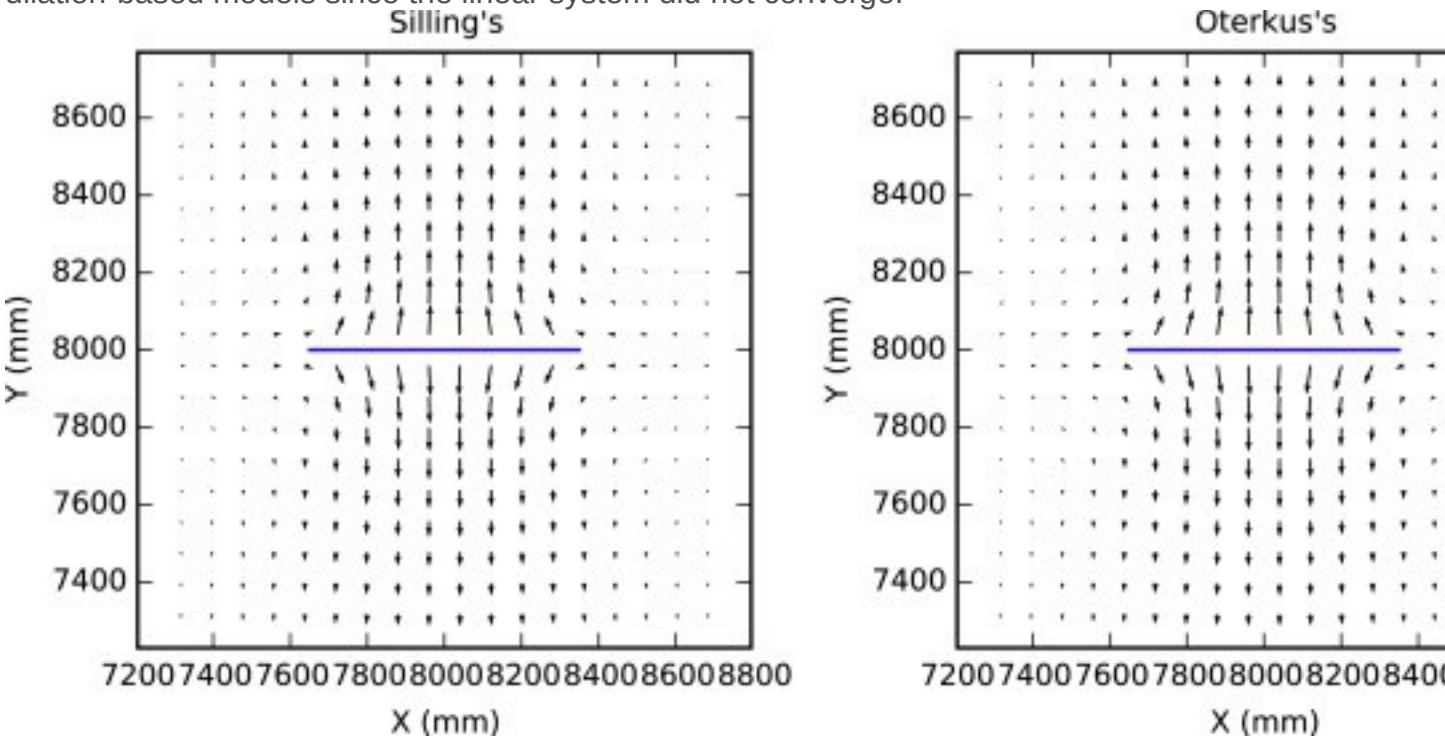

1. Download high-res image (356KB)
2. Download full-size image

Fig. 15. Displacement fields for the two dilation state based models. The scale on the displacement vectors is 75x the scale on the axes.

The errors for all four solutions are plotted in Fig. 16. (F is used as shorthand for deformation gradient in Table 8 and Fig. 16.) The jagged trend in the error is due to the geometric discretization of the crack mismatching the “true” crack geometry. The discrete material points are placed in a regular grid irrespective of the location of the crack endpoints. As the grid is refined, additional material points cross the crack tip. The error changes sharply when an additional set of material points pass the crack tip, causing a jump in the geometric error of the crack representation. This could be avoided by placing material points in a way to exactly match the endpoints of the crack.

However, this cannot be applied in crack growth problems where the position of the crack is unknown, so this trend should be included in the consideration of the error. Even though the errors are not observed to be decreasing smoothly, the convergence orders are estimated in Table 8 using the same regression procedure described in the previous section. Due to the non-smooth error trend, only the data after the regular jagged trend begins are used in the calculation, shown with markers on the line plots in Fig. 16. The obtained convergence orders are roughly linear for the deformation gradient-based model, but the data is not smooth enough to make any conclusion about the order of accuracy of the methods. It is, however, shown to be feasible to obtain an error that is less than 5% using the broken-bond representation of the thin pressurized crack.

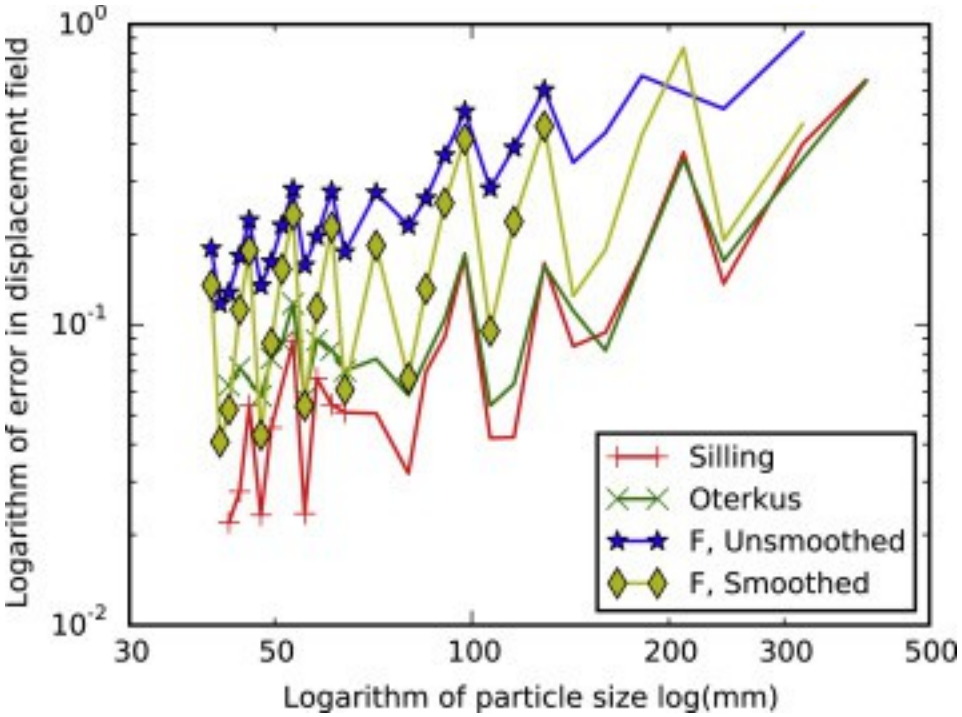

1. Download high-res image (341KB)
2. Download full-size image

Fig. 16. Error in the linear fracture mechanics problem as the particle size decreases for each of the models, including after smoothing the deformation gradient based solution.

Table 8. Rough order of convergence estimation in the linear fracture mechanics problem as the particle size decreases for each of the models, including after smoothing the deformation gradient based solution.

Method	Order	Min. error
Silling	**1.8022**	**2.2%**
Oterkus	0.4622	5.7%
F, unsmoothed	1.0200	11.7%

Method	Order	Min. error
F, smoothed	1.0836	4.1%

7. Conclusion

We rigorously examined the accuracy and convergence properties of the spatial discretization of three different peridynamic state-based force density laws with various forms of the influence function. We determined that a cubic influence function was consistently the best choice to guarantee convergence for each of the laws with varying horizon support radii. The deformation gradient model proposed by Silling, 2007 [19] is able to converge to the three constant-strain deformations at a linear rate. The two dilation-state based models are found to be unable to capture arbitrary constant strain modes: the method of Silling, 2007 [19] is only able to achieve linear convergence for the isotropic deformation mode, and the method of Oterkus, 2012 [23] is only able to achieve linear convergence for the simple shear mode.
However, the deformation gradient method suffers from instabilities in the displacement field solution. In the linear fracture mechanics problem, the instability is so great the artificial strains between points affect the critical bond-strain criteria for the fracture grown — indeed, this is the behavior that motivated this analysis. We demonstrated that a smoothing technique can adequately alleviate the instability issue, but the smoothed solution is still less accurate than the dilation state based models for the linear fracture mechanics problem. The error associated with the discretization of the crack prevents smooth decline of the solution errors, preventing conclusion on the rate of convergence. Even with these limitations on analysis, the peridynamic models are able to obtain less than 5% error in the domain integral of the displacement field.

Future work is merited on improving the accuracy and stability of the deformation gradient-based model. Bessa, 2014 [28] noted the coincidence of the deformation gradient based peridynamics model with a certain case of the strong-form Reproducing Kernel Particle Method (RKPM). Noting that the peridynamic formulation was improved with a smoothing operation, the underlying problem could be a matter of interpretation of the results. In RKPM, the solved degrees of freedom are the coefficients to an interpolating basis set without the delta function property. Using an underlying interpolation, unstable coefficients may produce a smooth solution after applied to the basis functions, although the instability may still be undesirable. Additionally, the interpolation function requires a different method of imposing Dirichlet boundary conditions than the coefficient-setting method used in this paper. As noted in Bessa,

2014, incorrect treatment of boundary conditions in many methods can initiate instabilities as well as introduce additional errors that reduce the order of convergence. In RKPM, Lagrange multipliers are typically used to enforce for Dirichlet boundary conditions and higher-order, stable approaches for Neumann boundary conditions are available. Thus, we hypothesize that there may be an underlying interpolation implied by the deformation-gradient based peridynamics formulation that could correctly interpret the oscillatory coefficients and provide insight into better ways of handling the boundary conditions.

Acknowledgments

This work was supported by Laboratory Directed Research and Development (LDRD) funding from Berkeley Lab, provided by the Director, Office of Science, of the U.S. Department of Energy under Contract No. DE-AC02-05CH11231.

Appendix. Differentiation

Tangent matrices to the peridynamics equations are required to solve the implicit equation efficiently. This is performed using a custom built code generation system built upon Sympy in Python. Two aspects to the peridynamics calculations make this type of code generation tricky: (1) a variable number of particles interacts with a particle, and (2) derivatives of quantities derived in for loops are needed for some calculations. The trick of unrolling the loops is not practical when each calculation can contain between 3 and about 30 particles, depending on the size of the horizon of the particle, which would require about 27 different implementations. This loop unrolling method could be used to produce a table of routines, but may end up required just-in-time compilation if another number of particles is needed. Instead, a single force and tangent routine is produced that propagates symbolic derivatives using chain rule through for loops, and is described as follows.

The dilation θ is the result of a summation over all the particle positions, so every force calculated depends on all of the particle positions. Now consider the case of generating the matrix and load vector for the interactions centered at one particle, indexed locally by 0, with L particles within its horizon, $Hx0$, each indexed by 1 to L locally. Care must be taken with respect to the derivatives of summations. If the differentiation argument contains the index of the summation, then a Kronecker delta-like process extracts a single term out of the summation. Otherwise, the resulting derivative is still a sum over its index. For the case of the dilation, where, with S standing in for the expression in Section 2.2,

(A.1)θ=∑k=1LSy0,yk
the derivative through the summation depends on the index of particle,
(A.2)∂θ∂yi=∂∂yi∑k=1LSy0,yk=∂S∂yky0,yik>1∑k=1L∂S∂y0y0,ykk=0.
For state-based peridynamics, the expressions are calculated at once for each point. Then, the derivative for a state-based peridynamics force is calculated in three parts using the chain rule, with
(A.3)dtidy0=∂ti∂y0+∂ti∂θ∑k=1L∂Sk∂y0
for the center-particle,
(A.4)dtidyi=∂t∂yi+∂ti∂θ∂Si∂yi
for the on-diagonal particle (that which is partaking in pair force), and
dtidyk=∂ti∂θ∂Sk∂yk
for the off-diagonal particles (those not partaking in the pair force, but still affecting the interaction through the state variables).
For the F-based peridynamic force, a matrix summation of N=∑k=1LSk is used. The procedure is the same as above, but a sum over each component of N is needed, so that the above three equations are, respectively,
(A.5)dtidy0=∂ti∂y0+∑a=12∑b=12∂ti∂Nab∑k=1L∂Sk,ab∂y0
for the center-particle,
(A.6)dtidyi=∂t∂yi+∑a=12∑b=12∂ti∂Nab∂Si,ab∂yi
for the on-diagonal particle, and
(A.7)dtidyk=∑a=12∑b=12∂ti∂Nab∂Sk,ab∂yk
for the off-diagonal particles. The above expressions are written as a sum over components rather than a double-index matrix contraction to express easily in Sympy. Each pair force thus yields a contribution two *full* block-rows in the local stiffness matrix of opposite signs:
(A.8)ki=dtidy0dtidyk=1...dtidyi...dtidyk=L0000⋮⋮⋮⋮0000−dtidy0−dtidyk=1...−dtidyi...−dtidyk=L0000⋮⋮⋮⋮.
Each entry in the above matrix represents a 2-by-2 block (or 3-by-3 in 3D). The first line of blocks corresponds to rows 0 and 1, and the second line to rows 2iand 2i+1. Each of these contributions is not symmetric, and each sub-block is not necessarily symmetric, due to the ∂θ∂y terms. Since this represents one pair force, all of the contributions for each pair have to be added together,
(A.9)klocal=∑i=1Lki.
After all of the stiffness matrix contributions of every particle within the horizon are added together, the resulting local matrix is symmetric, ensuring symmetry of the global stiffness matrix.

References

[1]

Silling Stewart A.**Reformulation of elasticity theory for discontinuities and long-range forces**
J. Mech. Phys. Solids, 48 (1) (2000), pp. 175-209
ArticleDownload PDFView Record in Scopus

[2]

Madenci Erdogan, Oterkus Erkan**Peridynamic Theory and its Applications**
Springer (2014)

[3]

Silling S.A., Weckner O., Askari E., Bobaru Florin**Crack nucleation in a peridynamic solid**
Int. J. Fract., 162 (1-2) (2010), pp. 219-227
CrossRefView Record in Scopus

[4]

Emmrich Etienne, Weckner Olaf, *et al.***On the well-posedness of the linear peridynamic model and its convergence towards the Navier equation of linear elasticity**
Commun. Math. Sci., 5 (4) (2007), pp. 851-864
CrossRefView Record in Scopus

[5]

Silling Stewart A, Lehoucq Richard B.**Convergence of peridynamics to classical elasticity theory**
J. Elasticity, 93 (1) (2008), pp. 13-37
CrossRefView Record in Scopus

[6]

Seleson Pablo, Parks Michael L., Gunzburger Max, Lehoucq Richard B.**Peridynamics as an upscaling of molecular dynamics**
Multiscale Model. Simul., 8 (1) (2009), pp. 204-227
CrossRefView Record in Scopus

[7]

Richard Becker and Richard J. Lucas, An assessment of peridynamics for pre and post failure deformation, 2011

[8]

Parks Michael L., Lehoucq Richard B., Plimpton Steven J., Silling Stewart A.**Implementing peridynamics within a molecular dynamics code**
Comput. Phys. Comm., 179 (11) (2008), pp. 777-783
ArticleDownload PDFView Record in Scopus

[9]

Seleson Pablo, Parks Michael**On the role of the influence function in the peridynamic theory**
Int. J. Multiscale Comput. Eng., 9 (6) (2011), pp. 689-706

CrossRefView Record in Scopus

[10]

Lai Xin, Ren Bo, Fan Houfu, Li Shaofan, Wu C.T., Regueiro Richard A., Liu Lisheng**Peridynamics simulations of geomaterial fragmentation by impulse loads**

Int. J. Numer. Anal. Methods Geomech., 39 (12) (2015), pp. 1304-1330

CrossRefView Record in Scopus

[11]

Ghajari M., Iannucci L., Curtis P.**A peridynamic material model for the analysis of dynamic crack propagation in orthotropic media**

Comput. Methods Appl. Mech. Engrg., 276 (2014), pp. 431-452

ArticleDownload PDFView Record in Scopus

[12]

Erkan Oterkus, Peridynamic theory for modeling three-dimensional damage growth in metallic and composite structures, The University of Arizona, 2010

[13]

Oterkus Erkan, Madenci Erdogan**Peridynamic analysis of fiber-reinforced composite materials**

J. Mech. Mater. Struct., 7 (1) (2012), pp. 45-84

CrossRefView Record in Scopus

[14]

Foster John T., Silling Stewart Andrew, Chen WAYNE W.**Viscoplasticity using peridynamics**

Internat. J. Numer. Methods Engrg., 81 (10) (2010), pp. 1242-1258

View Record in Scopus

[15]

Turner Daniel Z.**A non-local model for fluid-structure interaction with applications in hydraulic fracturing**

Int. J. Comput. Methods Eng. Sci. Mech., 14 (5) (2013), pp. 391-400

CrossRefView Record in Scopus

[16]

Oterkus Selda, Madenci Erdogan, Agwai Abigail**Peridynamic thermal diffusion**

J. Comput. Phys., 265 (2014), pp. 71-96

ArticleDownload PDFView Record in Scopus

[17]

Katiyar Amit, Foster John T., Ouchi Hisanao, Sharma Mukul M.**A peridynamic formulation of pressure driven convective fluid transport in porous media**

J. Comput. Phys., 261 (2014), pp. 209-229

ArticleDownload PDFView Record in Scopus

[18]

Ouchi Hisanao, Katiyar Amit, York Jason, Foster John T., Sharma Mukul M.**A fully coupled porous flow and geomechanics model for fluid driven cracks: a peridynamics approach**
Comput. Mech., 55 (3) (2015), pp. 561-576
CrossRefView Record in Scopus

[19]

Silling Stewart A., Epton M., Weckner O., Xu J., Askari E.**Peridynamic states and constitutive modeling**
J. Elasticity, 88 (2) (2007), pp. 151-184
CrossRefView Record in Scopus

[20]

Liu Wenyang, Hong Jung Wuk**Discretized peridynamics for linear elastic solids**
Comput. Mech., 50 (5) (2012), pp. 579-590
CrossRefView Record in Scopus

[21]

Gerstle Walter, Sau Nicolas, Silling Stewart**Peridynamic modeling of concrete structures**
Nucl. Eng. Des., 237 (12) (2007), pp. 1250-1258
ArticleDownload PDFView Record in Scopus

[22]

Le Q.V., Chan W.K., Schwartz J.**A two-dimensional ordinary, state-based peridynamic model for linearly elastic solids**
Internat. J. Numer. Methods Engrg., 98 (8) (2014), pp. 547-561
CrossRefView Record in Scopus

[23]

Oterkus Erkan, Madenci Erdogan**Ordinary state-based peridynamic material constants**
53rd AIAA/ASME/ASCE/AHS/ASC Structures, Structural Dynamics and Materials Conference 20th AIAA/ASME/AHS Adaptive Structures Conference 14th AIAA (2012), p. 1946

[24]

Bobaru Florin, Yang Mijia, Alves Leonardo Frota, Silling Stewart A., Askari Ebrahim, XuJifeng**Convergence, adaptive refinement, and scaling in 1D peridynamics**
Internat. J. Numer. Methods Engrg., 77 (6) (2009), pp. 852-877
CrossRefView Record in Scopus

[25]

Bobaru Florin, Ha Youn Doh**Adaptive refinement and multiscale modeling in 2D peridynamics**
J. Multiscale Comput. Eng., 9 (6) (2011), pp. 635-659
View Record in Scopus

[26]

Bobaru Florin, Hu Wenke**The meaning, selection, and use of the peridynamic horizon and its relation to crack branching in brittle materials**
Int. J. Fract., 176 (2) (2012), pp. 215-222
CrossRefView Record in Scopus

[27]

Silling Stewart A., Askari Ebrahim**A meshfree method based on the peridynamic model of solid mechanics**
Comput. Struct., 83 (17) (2005), pp. 1526-1535
ArticleDownload PDFView Record in Scopus

[28]

Bessa M.A., Foster J.T., Belytschko T., Liu Wing Kam**A meshfree unification: reproducing kernel peridynamics**
Comput. Mech., 53 (6) (2014), pp. 1251-1264
CrossRefView Record in Scopus

[29]

Michael L. Parks, Pablo Seleson, Steven J. Plimpton, Stewart A. Silling, Richard B. Lehoucq, Peridynamics with LAMMPS: A User Guide v0. 3 Beta, Sandia Report SAND2011-8523, Sandia National Laboratories, Albuquerque, NM, 2011

[30]

Littlewood David J.**Roadmap for Peridynamic Software Implementation, Technical Report SAND2015-9013, Sandia National Laboratories, Albuquerque, NM and Livermore, CA**
(2015)

[31]

Mitchell J.A., Parks M.L., Littlewood D.J., Silling S.A.**Peridigm Users' Guide, Technical Report SAND2012-7800, Sandia National Laboratories**
(2012)

[32]

SymPy Development Team, SymPy: Python library for symbolic mathematics, 2016

[33]

Van Der Walt Stefan, Colbert S. Chris, Varoquaux Gael**The NumPy array: a structure for efficient numerical computation**
Comput. Sci. Eng., 13 (2) (2011), pp. 22-30
CrossRefView Record in Scopus

[34]

Eric Jones, Travis Oliphant, Pearu Peterson, et al., SciPy: Open source scientific tools for Python, 2001. (Accessed 1 January 2016). http://www.scipy.org/

[35]

Pujii Akihiro, Nishida Akira, Oyanagi Yoshio**Evaluation of parallel aggregate creation orders: Smoothed aggregation algebraic multigrid method**

High Performance Computational Science and Engineering, Springer (2005), pp. 99-122
CrossRef

[36]

Hunter John D.**Matplotlib: A 2D graphics environment**
Comput. Sci. Eng., 9 (3) (2007), pp. 90-95
CrossRefView Record in Scopus

[37]

Westergaard H.**Bearing pressures and cracks**
J. Appl. Mech., 18 (1939)

[38]

Sneddon INa**The distribution of stress in the neighbourhood of a crack in an elastic solid**
Proceedings of the Royal Society of London A: Mathematical, Physical and Engineering Sciences, vol. 187, The Royal Society (1946), pp. 229-260
CrossRefView Record in Scopus

[1]

The equations in Le, 2014 [22] reduce to the same result upon recognizing that the term $\underline{w}\underline{e}\underline{d}\blacksquare\underline{x}=\int\underline{w}\underline{e}-\theta 3\underline{x}\underline{x}\underline{d}2x'=\int\underline{w}\underline{e}\underline{x}\underline{d}2x'-\theta 3\int\underline{w}\underline{x}\underline{x}\underline{d}2x'=\theta m2-\theta 3m=m6\theta$, where we have matched the underlined-state notation in Le.